Ultrasound Image Enhancement via Deconvolution

by

Dmitrii Govor
B.Sc., Pacific National University, 2019

A Report Submitted in Partial Fulfillment of the
Requirements for the Degree of

MASTER OF ENGINEERING

in the Department of Electrical and Computer Engineering

Ultrasound Image Enhancement via Deconvolution

by

Dmitrii Govor
B.Sc., Pacific National University, 2019

Supervisory
Committee

Dr. Daler Rakhmatov, Department of Electrical and Computer Engineering
Supervisor

Dr. Pan Agathoklis, Department of Electrical and Computer Engineering
Departmental Member

Abstract

Ultrasound imaging is a widespread medical imaging technique that is still a subject of active research. An important problem in ultrasound imaging is related to the effective use of deconvolution to improve the image quality. One of the ways to solve this problem is based on Robust Principal Component Analysis (RPCA), which requires some knowledge of the point spread function (PSF). Blind deconvolution (BD) refers to the situation when there is no prior knowledge of the PSF is available, and therefore, the latter needs to be estimated based on the given radio-frequency (RF) data. This report investigates the problem of blind deconvolution where the PSF being estimated can either be stationary or non-stationary. To evaluate the strengths and weaknesses of different deconvolution methods under consideration, we utilize two datasets corresponding to the PICMUS simulated phantom and the *in vivo* carotid artery, and apply multiple image quality indicators such as tissue-to-clutter ratio (TCR), contrast-to-noise ratio (CNR), full width at half maximum (FWHM), and others.

Table of Contents

Supervisory Committee ii
Abstract iii
Table of Contents iv
List of Tables vi
List of Figures vii
Acknowledgements ix
Dedication x

Chapter 1: Introduction 1
1.1 Medical Ultrasound Imaging 1
1.2 Ultrasound Imaging System 3
1.3 Point Spread Function 5
1.4 Deconvolution 6
1.5 Report Contribution and Organization 7

Chapter 2: Background 8
2.1 Iterative Reconstruction of Ultrasound Images Using Phase Updates 8
2.2 High-resolution and High-sensitivity Blood Flow Estimation 9
2.3 Blind Deconvolution and Robust Principal Component Analysis in Ultrasound Imaging 10
2.4 Modeling Non-stationary Blur in Ultrasound Imaging 12

Chapter 3: Considered Deconvolution Settings and Evaluation Cases 17
3.1. Deconvolution Settings 17
3.2. Evaluation Cases 18

Chapter 4: Evaluation Results 23
4.1. Evaluation Metrics 23
4.2. Case 1: Deconvolution Using Prestored Simulated PSF 25

4.3. Case 2: Deconvolution Using Estimated Stationary PSF 29
4.4. Case 3: Deconvolution Using Estimated Stationary PSF and RPCA ... 33
4.5. Case 4: Deconvolution Using Estimated Non-stationary PSF 41
4.6. Comparative Summary 45

Chapter 5: Conclusion and Future Work 50
5.1. Concluding Remarks 50
5.2. Future Directions 50

Bibliography 52

List of Tables

Table 1.1: Speed of sound in different materials 2
Table 3.1: Probe characteristics 19
Table 4.1: Image quality indicators for simulated phantom, Case 1 27
Table 4.2: Image quality indicators for carotid artery, Case 1..... 29
Table 4.3: Image quality indicators for simulated phantom, Case 2 31
Table 4.4: Image quality indicators for carotid artery, Case 2..... 33
Table 4.5: Image quality indicators for simulated phantom, Case 3 36
Table 4.6: Image quality indicators for carotid artery, Case 3..... 39
Table 4.7: Image quality indicators for a single- and three-iteration execution of BD-RPCA 41
Table 4.8: Image quality indicators for simulated phantom, Case 4 43
Table 4.9: Image quality indicators for carotid artery, Case 4..... 45
Table 4.10: Summary of image quality indicators for simulated phantom 46
Table 4.11: Summary of image quality indicators for carotid artery..... 48

List of Figures

Figure 1.1: Components of a typical ultrasound imaging system 4

Figure 1.2: The effect of the PSF on an image 6

Figure 3.1: Original B-mode images of the simulated phantom (a) and the carotid artery (b) before deconvolution 19

Figure 3.2: Prestored simulated PSFs used for PICMUS (a) and artery (b) RF data deconvolution. Estimated PSFs for PICMUS (c) and artery (d) RF data deconvolution 21

Figure 4.1: Background (1 and 2) and tissue (3) regions used for SNR and TCR calculations 25

Figure 4.2: B-mode images of the simulated phantom before (a) and after deconvolution using the prestored PSF with $p = 1.25$ (b), $p = 1.5$ (c), $p = 1.75$ (d) 26

Figure 4.3: B-mode images of the carotid artery before (a) and after deconvolution using the prestored PSF with $p = 1.25$ (b), $p = 1.5$ (c), $p = 1.75$ (d) 28

Figure 4.4: B-mode images of the simulated phantom before (a) and after deconvolution using the estimated PSF with $p = 1.25$ (b), $p = 1.5$ (c), $p = 1.75$ (d) 30

Figure 4.5: B-mode images of the carotid artery before (a) and after deconvolution using the estimated PSF with $p = 1.25$ (b), $p = 1.5$ (c), $p = 1.75$ (d) 32

Figure 4.6: B-mode images of the simulated phantom before (a) and after deconvolution using the estimated PSF and RPCA algorithm with $\lambda = 0.375, \rho = 0.5, \mu = 10^{-6}$ (b), $\lambda = 0.0375, \rho = 0.5, \mu = 10^{-6}$ (c), $\lambda = 3.75, \rho = 0.5, \mu = 10^{-6}$ (d), $\lambda = 0.375, \rho = 0.05, \mu = 10^{-6}$ (e), $\lambda = 0.375, \rho = 5, \mu = 10^{-6}$ (f), $\lambda = 0.375, \rho = 0.5, \mu = 10^{-10}$ (g), and $\lambda = 0.375, \rho = 0.5, \mu = 10^{-2}$ (h) 35

Figure 4.7: B-mode images of the carotid artery before (a) and after deconvolution using the estimated PSF and RPCA algorithm with $\lambda = 0.0003, \rho = 1, \mu = 10^{-8}$ (b), $\lambda = 0.00003, \rho = 1, \mu = 10^{-8}$ (c), $\lambda = 0.003, \rho = 1, \mu = 10^{-8}$ (d), $\lambda = 0.0003, \rho = 0.05, \mu = 10^{-8}$ (e), $\lambda = 0.0003, \rho = 20, \mu = 10^{-8}$ (f), $\lambda = 0.0003, \rho = 1, \mu = 10^{-12}$ (g), and $\lambda = 0.0003, \rho = 1, \mu = 10^{-4}$ (h) 38

Figure 4.8: B-mode images of the carotid artery after deconvolution using one (a) and three (b) iterations of the BD-RPCA algorithm 40

Figure 4.9: B-mode images of the simulated phantom before (a) and after deconvolution using an estimated non-stationary PSF with $p = 1.25$ (b), $p = 1.5$ (c), $p = 1.75$ (d) 42

Figure 4.10: B-mode images of the carotid artery before (a) and after deconvolution using an estimated non-stationary PSF with $p = 1.25$ (b), $p = 1.5$ (c), $p = 1.75$ (d) 44

Figure 4.11: TCR values for region 1 and region 2 48

Acknowledgements

I would like to express my sincere gratitude to my supervisor Dr. Daler Rakhmatov who opened the door for me into my future and supported me throughout the whole program. I would also like to thank Dr. Pan Agathoklis, who helped me to become more confident in my teaching skills and was always kind to me during our work together, for his help with examining my work as a committee member.

Dedication

I dedicate this work to my wife, parents, and grandparents for their never-ending love and support. Without you all, none of this would have been made possible, thank you.

Chapter 1: Introduction

1.1. Medical Ultrasound Imaging

Ultrasound imaging is a non-invasive and cost-effective medical imaging technique that allows one to examine internal organs without the need of surgical procedures. Consequently, this highly valuable diagnostic technique attracts the significant interest from the research community. It is clearly important to be able to create accurate and clear images in order to diagnose and treat patients with the early stages of cancer, tumors, and other serious diseases.

To understand better the working principles of ultrasound imaging systems, it is important to recall some fundamentals of ultrasound. Ultrasound is defined as sound waves with frequencies above 20,000 Hz and therefore not perceivable by human ears [1]. These sound waves are transmitted through some tissues and reflected back to the transducer [2]. These waves can be described in the following way [3], [4]:

$$\left[\Delta - \frac{1}{c^2}\frac{\partial^2}{\partial t^2}\right] p(\vec{r}, t) = 0, \tag{1}$$

where p is the wave function of space and time, Δ is the Laplace operator, and c is the speed of sound [5].

The speed of sound varies depending on the material it travels through. To calculate the speed, one can use the following formula [4], [6]:

$$c = \sqrt{\frac{1}{\rho\kappa}}, \tag{2}$$

where ρ is the mass density and κ is the compressibility. Table 1.1 shows the speed of sound in different materials.

Table 1.1. Speed of sound in different materials [4], [7].

Material	**Density, ρ, $\frac{\mathbf{kg}}{\mathbf{m^3}}$**	**Speed of sound, c, $\frac{\mathbf{m}}{\mathbf{s}}$**
Air	1.2	330
Fat	920	1450
Soft tissue	1027	1540
Brain	1030	1541
Liver	1060	1549
Kidney	1040	1561
Blood	1060	1570
Muscle	1070	1585
Bone	1380-1810	4080

There are multiple modes and techniques that are able to capture the interaction between ultrasound waves and tissues [2]. Some of the most frequently used ones include [8], [9]:

- A-mode, also known as *amplitude mode*, is considered to be the simplest ultrasound technique with a single transducer scanning one single line through the body and producing a plot of echo amplitudes as a function of depth [10], [11].
- B-mode, or *brightness mode*, is the most common mode of ultrasound imaging. It involves transducers scanning a plane of tissue and providing its two-dimensional image. Because of this fact it is also called 2D mode [11], [12], [13].
- C-mode in its functionality is close to B-mode, also producing a two-dimensional image. It combines both A-mode and B-mode to pick data from a certain depth and plot a two-dimensional image slice at the chosen depth [9], [11], [14].
- M-mode, or *motion mode*, operates continuously throughout time. The transducer continuously emits pulses taking a number of either A-mode or B-mode images, thus producing a so-called “video” of ultrasound. It is often used for velocity estimation [11], [15].
- Doppler mode uses the Doppler effect to visualize blood flow, and estimate its

velocity and directions [16].

1.2. Ultrasound Imaging System

Ultrasound imaging systems are commonly used in modern medical imaging applications [17], [18], [19]. A typical diagram of such systems can be seen in Figure 1.1. The ultrasound waves are transmitted by the transducer into a region of interest, after which the transducer switches to the reception mode. The transducer plays one of the biggest roles in the whole system, since it is responsible for producing ultrasound waves via converting them from the electrical energy in the transmission mode, and vice versa in the reception mode [20]. It typically consists of 64 to 256 piezo-electric elements and is able to generate either focused waves, plane waves, or diverging waves [5]. When the transmitted wave propagates through the tissues, it encounters materials with different densities. Whenever a transmitted wave encounters these changes in density, a reflected wave is produced.

In receiving mode, the transducer receives the reflected sound waves and converts them back to electrical signals. These electrical signals, called analog radio frequency (RF) signals, are amplified, and then sampled and quantized into digital RF signals [21]. Next, the beamformer control unit synchronizes the transmitted signal with the received signal to compensate for the time it took for the signal to travel to the tissues and back. After that, depending on the imaging mode, the digital RF signals pass through different image preprocessing and reconstruction modules. For this report, we are mostly interested in B-mode, where beamformed RF signals undergo envelope detection and logarithmic compression [9]. In some cases, the final image is subjected to additional filtering and scan conversion that provide overall image enhancement and ensure the fit for the desired display system [22], [23].

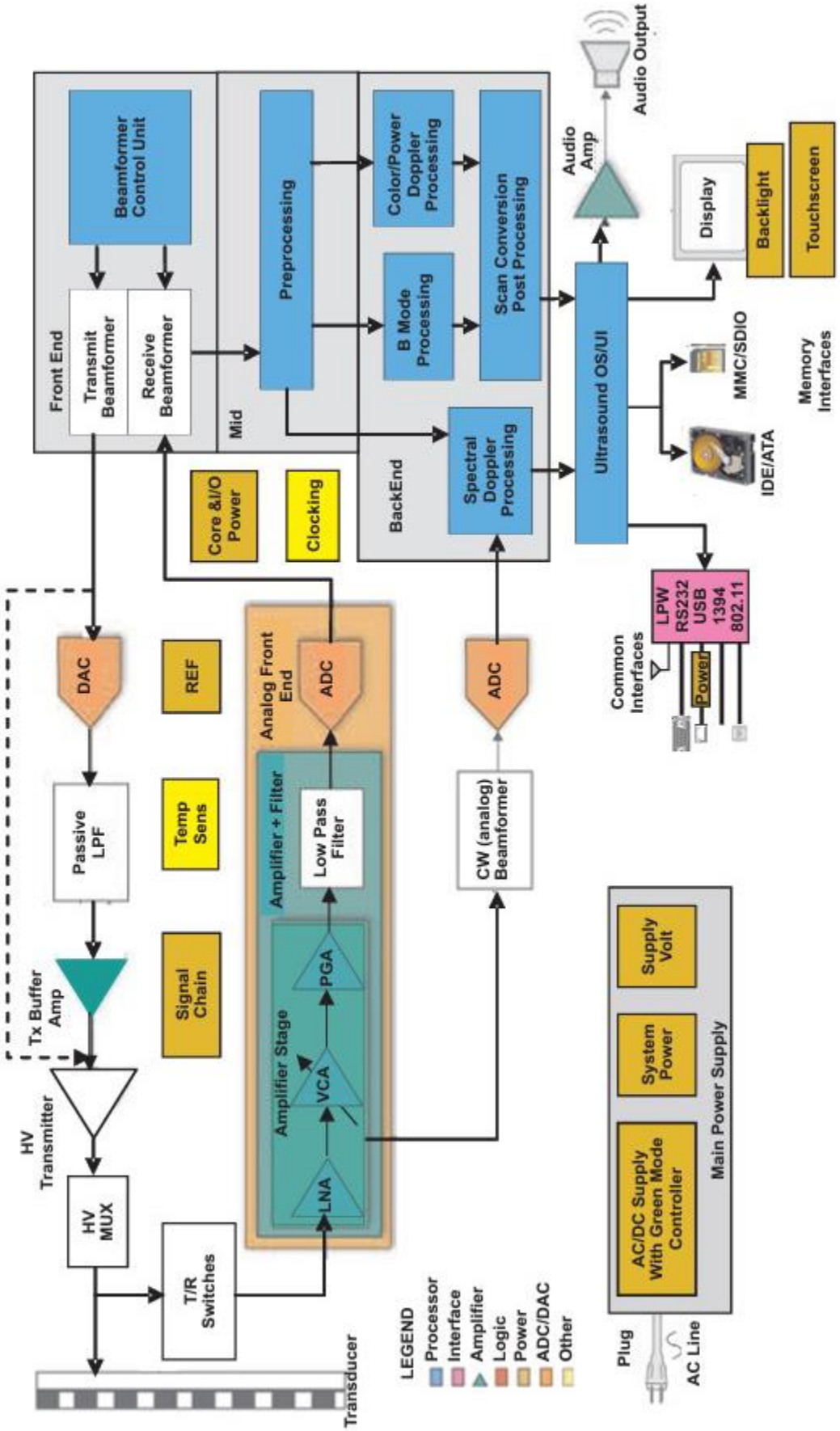

Figure 1.1. Components of a typical ultrasound imaging system [22].

1.3. Point Spread Function

The Point Spread Function (PSF) is a function that characterizes a response of an imaging system to a point source [24]. It can also be interpreted as an impulse response of an imaging system. An ultrasound image can be viewed as a result of convolution [25] of the PSF of the ultrasound imaging system and the tissue-reflectivity function (TRF) [26], [27]. Convolution is an operator that takes two signals and produces a third signal as a combination of them [28], [29]. 2D convolution can be described in the following way:

$$Z(i,j) = X(i,j) \circledast Y(i,j) = \sum_{n_1=-\infty}^{\infty} \sum_{n_2=-\infty}^{\infty} X(n_1, n_2) * Y(i - n_1, j - n_2), \qquad (3)$$

where X is the first 2D signal, Y is the second 2D signal, Z is the resulting 2D signal, i and j are the indices of the element being calculated, while n_1 and n_2 represent the offset. The outcome of such convolution is illustrated in Figure 1.2.

One of the common models of ultrasound images is based on the following formula [30]:

$$M = F \circledast \mathcal{H} + N, \qquad (4)$$

where M is a 2D image data after beamforming, F is the TRF, $\mathcal{H}$ is the PSF, N is noise, and $\circledast$ denotes convolution. Deconvolution refers to finding F given M and $\mathcal{H}$.

The PSF of an ultrasound imaging system is an essential factor affecting the performance of the whole system and the quality of the output images [31]. Unfortunately, sometimes it can be problematic to obtain a correct PSF that accurately captures the impulse response of the ultrasound imaging system [32]. PSF estimation plays a crucial role in algorithms that aim to recover an original image before it was affected by the PSF.

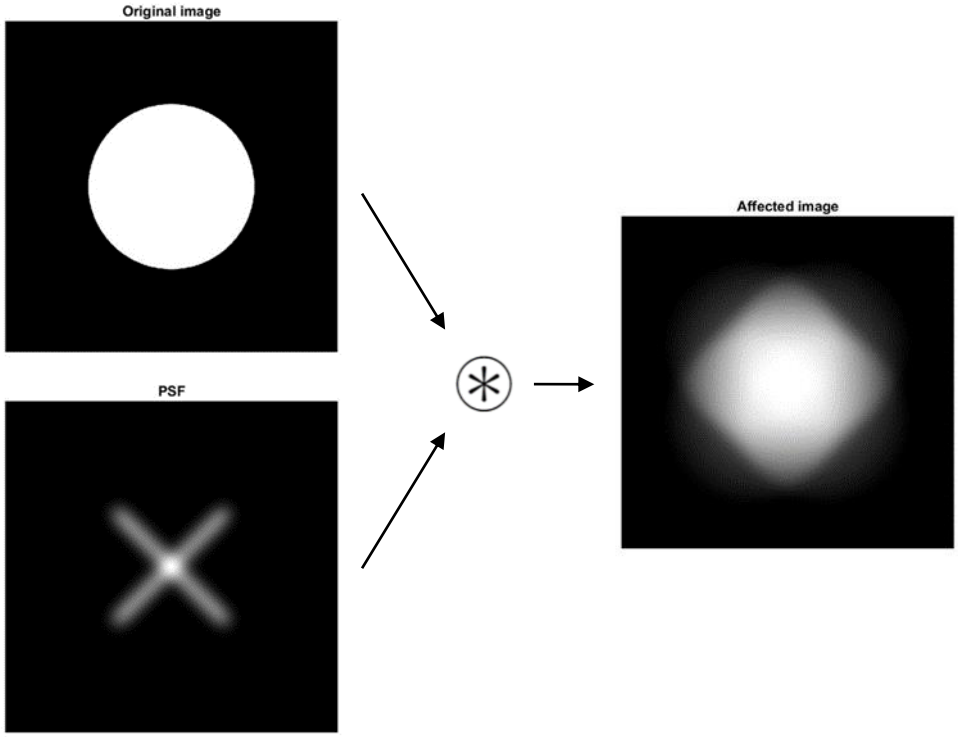

Figure 1.2. The effect of the PSF on an image.

1.4. Deconvolution

Deconvolution essentially reverses the action of a convolution operator. It is also sometimes called deblurring. The basis for the deconvolution was laid out more than seven decades ago by N. Wiener in his book “Extrapolation, Interpolation, and Smoothing of Stationary Time Series: with Engineering Applications” in 1949 [33].

Nowadays, the concept of deconvolution is widely used in ultrasound imaging. One of its main purposes is to recover an original image by removing the PSF effects from it [34]. Depending on the knowledge of the PSF most methods for deconvolution can be divided into two different groups: non-blind and blind deconvolution [17]. Commonly, non-blind deconvolution outperforms blind deconvolution, provided that the PSF is known exactly in advance, which can be a hard or even impossible requirement to meet [35], [36], [37]. On the other hand, blind deconvolution requires no prior knowledge and

estimates the PSF solely based on the affected image [38], [39], [40]. This is the type of deconvolution we are exploring in this report. Some of the works related to blind deconvolution that formed the basis of our approach are described in Section 2.

1.5. Report Contribution and Organization

The key motivation for this work was the paper [41] by A. Besson *et al*. in which the authors solve the problem of blind deconvolution by introducing a non-stationary PSF operator. The disadvantage of a non-stationary PSF is mainly due to its significant computational cost. On the other hand, the paper [42] written by D. Pham *et al*. proposes a Blind Deconvolution and Robust Principal Component Analysis (BD-RPCA) algorithm for deconvolving 3D Doppler data using a stationary PSF. Our goal was to adapt the algorithm proposed in [42] so that it would be able to work with 2D beamformed RF data at a low computational cost while preserving the image quality level set by the deconvolution approach using a non-stationary PSF. Our reported evaluation results explore the benefit of non-stationary versus stationary blur modeling, using the B-mode images of the PICMUS simulated phantom and the *in vivo* carotid artery [41].

The rest of this report is organized as follows. Chapter 2 introduces the works that formed the theoretical basis for the presented results. This chapter covers such concepts as the iterative reconstruction of ultrasound images by means of blind deconvolution, blood flow estimation based on Doppler data, ultrasound image enhancement using the BD-RPCA algorithm, and the principles of non-stationary PSF modeling. Then, Chapter 3 gives technical details about our deconvolution settings used in various evaluation cases. Next, Chapter 4 discusses examples of deconvolved images and the corresponding numerical evaluation metrics. Finally, Chapter 5 provides concluding remarks and outlines some possible directions for future work.

Chapter 2: Background

2.1. Iterative Reconstruction of Ultrasound Images Using Phase Updates

The basis for the BD-RPCA algorithm takes its roots in the paper [43] written by O. Michailovich *et al*, where the authors address a problem of image deconvolution being extremely sensitive to errors that can occur during estimation of the PSF. To solve this problem, the paper [43] proposes a new method of blind deconvolution for ultrasound images that estimates the TRF directly from the corresponding beamformed RF data [43]. As it is mentioned in [43] and Section 1.4, a large portion of the methods that address the problem of deconvolution can be divided into two different approaches that differ in the way the PSF is handled. The first approach suggests obtaining an estimate of the PSF on the first step, followed by image enhancement by a means of non-blind deconvolution [44], [45]. An example of such an approach is deconvolutive RPCA (DRPCA), which is computationally inexpensive. The second approach suggests recovering the PSF iteratively while deconvolving the image. The paper [43] attempts to combine these two approaches through the formulation of an inverse problem.

As discussed in Section 1.3, a common model for ultrasound images can be represented by the equation (4). In the case of blind deconvolution, the PSF is unknown and the only input is the matrix M. However, it is possible to make assumptions that are "encoded" in the behavior of properly defined real-valued functionals φ and ψ that attain relatively small values for the admissible TRF (F) and estimated PSF ($\mathcal{H}_e$), respectively [43]. Taking this into consideration, one can formulate a problem of blind deconvolution as the following optimization problem:

$$\left[\widehat{\mathcal{H}}_e, \hat{F}\right] = \arg\min_{\mathcal{H}_e, F} \left\{ \frac{1}{2} \left| |F \circledast \mathcal{H}_e - M| \right|_F^2 + \varphi(F) + \psi(\mathcal{H}_e) \right\}, \tag{5}$$

where $\left|\left|\cdot\right|\right|_F$ denotes the Frobenius norm. The formulated problem can be solved utilizing alternating minimization [46].

To approach this problem, it is assumed that in addition to the image M one possesses partial information on the PSF, namely the magnitude $\widetilde{H}$ of its Discrete Fourier Transform $\mathcal{F}: \mathcal{H}_e \to \widetilde{H}$. The latter can be calculated from M using homomorphic filtering [44]. Under these assumptions, the minimization problem can be reformulated as

$$\left[\widehat{\mathcal{H}}_e, \hat{F}\right] = \arg\min_{\mathcal{H}_e, F} \left\{ \frac{1}{2} \left| |F \circledast \mathcal{H}_e - M| \right|_F^2 + \varphi(F) \right\}, s.t. |\mathcal{F}(\mathcal{H}_e)| = \widetilde{H}. \tag{6}$$

It can now be solved by iteratively alternating between F and $\mathcal{H}_e$:

$$\left[\hat{F}^{(k+1)}\right] = \arg\min_{F} \left\{ \frac{1}{2} \left| \left| F^{(k)} \circledast \mathcal{H}_e^{(k)} - M \right| \right|_F^2 + \varphi\left(F^{(k)}\right) \right\}, \tag{7}$$

$$\left[\widehat{\mathcal{H}}_e^{(k+1)}\right] = \arg\min_{\mathcal{H}_e} \left\{ \left| \left| F^{(k+1)} \circledast \mathcal{H}_e^{(k)} - M \right| \right|_F^2 \right\}, s.t. |\mathcal{F}(\mathcal{H}_e)| = \widetilde{H}. \tag{8}$$

In this particular case, φ is chosen to be the Huber function:

$$\varphi(F) = \gamma \sum_{p=0}^{P-1} \sum_{q=0}^{Q-1} \begin{cases} |F_{p,q}|^2, & |F_{p,q}| \le a \\ 2a|F_{p,q}| - a^2, & |F_{p,q}| > a \end{cases}, \tag{9}$$

where $\gamma > 0$ is a regularization parameter, $a > 0$ is some fitting constant, and P and Q correspond to the dimensions of F.

2.2. High-resolution and High-sensitivity Blood Flow Estimation

Another remarkable paper that has served as a basis for the BD-RPCA algorithm is [47] written by H. Shen *et al.*, which suggests performing deconvolution of the blood flow based on RPCA using the augmented Lagrangian-based alternating direction method of multipliers (ADMM) described in [46]. In this paper, the authors employ a Casorati

matrix S and the PSF $\mathcal{H}$ as the input for their proposed non-blind deconvolution algorithm. Casorati matrix is a matrix constructed from 3D Doppler data modeled as

$$S = T + X + N, \tag{10}$$

where T, X, and N are tissue, blood, and noise components, respectively. All these matrices belong to the set $\mathbb{C}^{N_z N_x \times N_t}$, where N_t is the number of individual data frames of size $N_x \times N_z$ acquired over the time interval of interest.

The paper [47] proposes to find X and T by solving the following optimization problem:

$$[\hat{X}, \hat{T}] = \arg\min_{X,T} \left\{ ||S - \mathcal{H} \circledast X - T||_F^2 + \lambda ||X||_1 + \rho ||T||_* \right\}, \tag{11}$$

where $||\cdot||_*$ denotes the nuclear norm [66], $\mathcal{H}$ is the PSF, and $\lambda, \rho > 0$ are two hyperparameters balancing a tradeoff between sparsity of the blood component and low-rankness of the tissues component [47], [48]. This is a convex optimization problem [67] that can be solved using an ADMM-based algorithm [47].

The described approach is called deconvolutive RPCA (DRPCA). As mentioned previously, it requires the knowledge of the corresponding PSF, which can be considered as the main drawback of this method. It should be noted, that in (11) only X is being deconvolved because we are only interested in the high-resolution blood component X, while the low-resolution tissue component T is simply ignored (as a deconvolution target) despite being affected by the PSF as well [47].

2.3. Blind Deconvolution and Robust Principal Component Analysis in Ultrasound Imaging

The third paper [42] written by D. Pham *et al.* introduces the BD-RPCA algorithm which can perform deconvolution of blood flow without any prior knowledge of the PSF.

As an input, this algorithm uses a Casorati matrix S according to the model described by (10). The PSF is considered to be unknown and, therefore, the problem described in [47] turns into a problem of blind deconvolution.

The objective of [42] is to estimate a high-resolution blood flow component X alongside with a tissue component T and the PSF $\mathcal{H}_e$ from 2D ultrasound Doppler signals [42]. This method is based on the previously described blind deconvolution [43] and DRPCA [47] methods, combining them into the following optimization problem:

$$\left[\hat{X}, \hat{\mathcal{H}}_e, \hat{T}\right] = \arg\min_{X,\mathcal{H}_e,T} \left\{ \left|\left|S - \mathcal{H}_e \circledast X - T\right|\right|_F^2 + \lambda \left|\left|X\right|\right|_1 + \rho \left|\left|T\right|\right|_* \right\}, \quad s.t. \left|\mathcal{F}(\mathcal{H}_e)\right| = \widetilde{H}. \tag{12}$$

This type of optimization problem can be solved by applying an alternating algorithm that involves two separate steps:

1) First, $\mathcal{H}_e$ is fixed which leads to (12) changing its form to

$$\left[\hat{X}^{(k+1)}, \hat{T}^{(k+1)}\right] = = \arg\min_{X,T} \left\{ \left|\left|S - \mathcal{H}_e^{(k)} \circledast X^{(k)} - T^{(k)}\right|\right|_F^2 + \lambda \left|\left|X^{(k)}\right|\right|_1 + \rho \left|\left|T^{(k)}\right|\right|_* \right\}. \tag{13}$$

   This step applies an RPCA algorithm to produce estimated $\hat{X}$ and $\hat{T}$.

2) In the second step, X and T are fixed, and $\mathcal{H}_e$ is assumed to be spatiotemporally invariant and equal to the temporal mean of all clutter filtered frames found previously [42]. Using the distributive property of the convolution, (12) can be expressed in the following way:

$$\left[\hat{\mathcal{H}}_e^{(k+1)}\right] = \arg\min_{\mathcal{H}_e} \left\{ \left|\left| \overline{\sum_{N_t}} \left(S - T^{(k+1)}\right) - \mathcal{H}_e^{(k)} \circledast \overline{\sum_{N_t}} \left(X^{(k+1)}\right) \right|\right|_F^2 \right\}, \quad s.t. \left|\mathcal{F}\left(\mathcal{H}_e^{(k)}\right)\right| = \widetilde{H}, \tag{14}$$

   where $\overline{\Sigma}_{N_t}(Z)$ denotes a temporal mean of a 2D matrix Z. This problem can be

solved by using the previously described BD algorithm ignoring the estimation of $\overline{\Sigma}_{N_t}\left(X^{(k+1)}\right)$.

It is important to mention that the RPCA algorithm is also used in the beginning to initialize $X^{(0)}$ and $T^{(0)}$. This step allows to speed up the convergence of the proposed algorithm. Putting it all together, Algorithm 1 shown below summarizes the BD-RPCA method under consideration.

Algorithm 1: BD-RPCA [42].

Input: observed Casorati matrix S

Initialize: $tol = 10^{-6}, \left[\hat{X}^{(0)}, \hat{T}^{(0)}\right] = \text{RPCA}(S)$

while $\left|\left|\hat{X}^{(k+1)} - \hat{X}^{(k)}\right|\right|_F > tol$ **do**

1) compute temporal mean: $A_{ST}^{(k+1)} = \overline{\Sigma}_{N_t}\left(S - \hat{T}^{(k)}\right)$

2) estimate PSF: $\left[\widehat{\mathcal{H}}_e^{(k+1)}\right] = \text{BD}\left(A_{ST}^{(k+1)}\right)$

3) update $\left[\hat{X}^{(k+1)}, \hat{T}^{(k+1)}\right] = \text{DRPCA}\left(S, \widehat{\mathcal{H}}_e^{(k+1)}\right)$

end

Output: high-resolution blood component $\hat{X}$ and estimated PSF $\widehat{\mathcal{H}}_e$.

2.4. Modeling Non-stationary Blur in Ultrasound Imaging

The paper [41] written by A. Besson *et al.* deals with the modeling of a non-stationary PSF. In this paper, authors use $L_2(\Omega)$ to denote the Hilbert space of the square-integrable functions that take values in a space Ω. The inner product of two functions $f, g \in L_2(\Omega)$ is denoted by $\langle f, g \rangle_{L_2(\Omega)}$. The adjoint of a linear operator $\mathcal{H}: L_2(\Omega_1) \mapsto L_2(\Omega_2)$ is expressed as $\mathcal{H}^\dagger: L_2(\Omega_2) \mapsto L_2(\Omega_1)$ [41]. The symbol $X^\dagger$ is the Hermitian transpose of a matrix $X \in \mathbb{R}^{U \times V}$ with U rows and V columns. A sub-matrix of X with the restriction to v columns indexed by the set $J \subset \{1, \ldots, v\}$ is denoted by $X_{\bullet J}$. The operation $X \circ Y$ is the element-wise product between the two matrices X and Y.

The measurements obtained by a set of transducer elements located at positions

$(p_i)_{i=1}^{N_{el}}, p_i \in \mathbb{R}^2$ are denoted by

$$m(t) = \left[m_1(t), \dots, m_{N_{el}}(t)\right] \in L_2([0,T])^{N_{el}}, \tag{15}$$

where $m_i(t)$ are echo signals, $t \in [0,T]$ is the measurement time interval, N_{el} is the number of transducer elements, and $L_2([0,T])^{N_{el}} := L_2([0,T]) \times \dots \times L_2([0,T])$. The TRF is denoted by $\gamma \in L_2(\Omega)$.

The authors also introduce three operators that capture the main ultrasound imaging processes. The first one is the propagation operator $\mathcal{H}: \gamma \mapsto m$ that relates the measurements $m(t)$ and the TRF γ by the following equation:

$$m_i(t) = \int_{r \in \Omega} o(p_i, r) v_{pe}\big(t - \tau(r, p_i)\big)\gamma(r) dr\,, \tag{16}$$

where r is the location at which the TRF is being estimated, $o(p_i, r)$ accounts for the spatial directivity and decay of the reflected wave, $v_{pe}(t)$ is the pulse-echo waveform [49], and $\tau(r, p_i)$ is the round-trip travel time of the signal given by

$$\tau(r, p_i) = t_{Tx}(r) + t_{Rx}(r, p_i), \tag{17}$$

where $t_{Rx}(r, p_i) = \frac{||r - p_i||_2}{c}$ is the propagation delay along the receive path with c being the speed of sound, and $t_{Tx}(r)$ is the propagation delay along the transmit path of the signal propagation. Equation (16) for all N_{el} measurements can be compactly expressed as

$$m(t) = \mathcal{H}\{\gamma\}(t). \tag{18}$$

The second operator, $\mathcal{D}: m \mapsto g$, is referred to as the delay-and-sum (DAS) operator, used in the process of receive beamforming. During this process the RF image g, which is an estimate of the TRF γ, is reconstructed from the measurements $m(t)$ in accordance with the following equation:

$$g(r) = \sum_{i=1}^{N_{el}} a(p_i, r) m_i\big(\tau(r, p_i)\big)\,, \tag{19}$$

where $a(p_i, r)$ represents the aperture-apodization weights. This operation can be rewritten in the following integral form:

$$g(r) = \int_0^T \sum_{i=1}^{N_{el}} a(p_i, r)\delta\big(t - \tau(r, p_i)\big)m_i(t)\, dt = \mathcal{D}\{m\}(r). \tag{20}$$

Putting it all together, one can specify the entire ultrasound imaging procedure as a mapping between the true TRF γ and its corresponding beamformed RF image g [41]

$$\gamma \mapsto g = \mathcal{D}\mathcal{H}\{\gamma\} \tag{21}$$

The third operator $\mathcal{K}: L_2(\Omega) \mapsto L_2(\Omega)$, known as the PSF operator, describes the blur that is introduced in the process of the TRF reconstruction. Taking equations (16) and (19) into consideration, the PSF operator can be used in the following way:

$$g(r) = \int_{s \in \Omega} \left(\sum_{i=1}^{N_{el}} a(p_i, r)o(p_i, s)v_{pe}\big(\tau(r, p_i) - \tau(s, p_i)\big) \right) \gamma(s)ds = \mathcal{K}\{\gamma\}(r). \tag{22}$$

As the result, the reconstruction problem can now be defined as follows:

$$\text{Recover } \gamma \text{ from } g = \mathcal{K}\{\gamma\}. \tag{23}$$

To discretize the continuous problem above, the authors of [41] replace the TRF γ with its discrete counterpart Γ defined over a regular $N_x \times N_z$ grid as a data matrix from the set $\mathbb{R}^{N_x \times N_z}$. On the other hand, the discrete version of the beamformed RF data g is defined as a matrix $G \in \mathbb{R}^{\widehat{N}_x \times \widehat{N}_z}$ over a regular $\widehat{N}_x \times \widehat{N}_z$ grid. Similarly, we have

$$\mathcal{K} = \mathcal{D}\mathcal{H} \to K = DH, \tag{24}$$

where $H: \mathbb{R}^{N_x \times N_z} \mapsto \mathbb{R}^{N_t \times N_{el}}$, $D: \mathbb{R}^{N_t \times N_{el}} \mapsto \mathbb{R}^{\widehat{N}_x \times \widehat{N}_z}$, and $K: \mathbb{R}^{N_x \times N_z} \mapsto \mathbb{R}^{\widehat{N}_x \times \widehat{N}_z}$. Given these discretized operators, the corresponding reconstruction problem can now be stated as follows:

$$\text{Recover } \Gamma \text{ from } G = K\Gamma \tag{25}$$

For the sake of simplicity, both G and Γ are assumed to be defined over the same grid, meaning that $N_x = \widehat{N}_x$ and $N_z = \widehat{N}_z$.

To solve the above problem, one can first express the composition of discretized H and Γ in the following form:

$$H\Gamma = V_{pe}\left[\sum_{j=1}^{N_x} W_j \circ I_j\Gamma_{\bullet j}\right] \in \mathbb{R}^{N_t \times N_{el}}, \tag{26}$$

where the weighting matrix $W_j \in \mathbb{R}^{N_t \times N_{el}}$ is defined element-wise as $\left(W_j\right)_{li} = w_j(p_i, t_l)$, $V_{pe} \in \mathbb{R}^{N_t \times N_t}$ is the Toeplitz matrix associated with the discrete convolution with the pulse-echo waveform $v_{pe} \in \mathbb{R}^{N_t}$, and $I_j \colon \mathbb{R}^{N_z} \mapsto \mathbb{R}^{N_t \times N_{el}}$ denotes N_x interpolation operators such that

$$\gamma\left(r\left(\alpha_j, p_i, t_l\right)\right) \approx \left(I_j\Gamma_{\bullet j}\right)_{li}, j = 1, \dots, N_x, \tag{27}$$

where $r\left(\alpha_j, p_i, t_l\right) = [\alpha, z(\alpha, p_i, t)]^T$ arises from an appropriate reparametrization detailed in [41], [50]. Equation (26) essentially conveys that

$$(H\Gamma)_{li} \approx \left(V_{pe}\widehat{m}_i\right)_l, l = 1, \dots, N_t, \tag{28}$$

where

$$\widehat{m}_i(t_l) = \sum_{j=1}^{N_x} w_j(p_i, t_l)\gamma\left(r\left(\alpha_j, p_i, t_l\right)\right) \tag{29}$$

Next, one can introduce the adjoint propagation operator $H^\dagger$ defined in the following way:

$$H^\dagger M' = \sum_{i=1}^{N_{el}} O_i \circ I_i'\left(V_{pe}^T M'_{\bullet i}\right) \in \mathbb{R}^{N_x \times N_z}, \tag{30}$$

where $O_i \in \mathbb{R}^{N_x \times N_z}$ is defined element-wise as $(O_i)_{sq} = o\left(p_i, r_{sq}\right)$ to account for spatial directivity and decay of the reflected wave, with $r_{sq} = \left(x_s, z_q\right), s = 1, \dots, N_x$, and $q = 1, \dots, N_z$. Symbol $I_i' \colon \mathbb{R}^{N_t} \mapsto \mathbb{R}^{N_x \times N_z}$ denotes N_{el} interpolation operators such that

$$\widetilde{m}_i\left(\tau\left(r_{sq}, p_i\right)\right) \approx \left(I_i'\left(V_{pe}^T M'_{\bullet i}\right)\right)_{sq}, i = 1, \dots, N_{el}, \tag{31}$$

where $\widetilde{m}_i(t) = v_{pe}(-t) *_t m_i(t)$. Matrix M' is the measured raw RF data that can be

expressed as $M' = H\Gamma \in \mathbb{R}^{N_t \times N_{el}}$.

Finally, the discretized DAS operator D can be written as

$$DM' = \sum_{i=1}^{N_{el}} A_i \circ I_i' M'_{\bullet i} \in \mathbb{R}^{N_x \times N_z}, \tag{32}$$

where $A_i \in \mathbb{R}^{N_x \times N_z}$ is defined element-wise as $(A_i)_{sq} = a(p_i, r_{sq})$ to account for the aperture-apodization weights. The discretized adjoint DAS operator $D^\dagger$ can then be expressed as

$$D^\dagger \Gamma = \sum_{j=1}^{N_x} W_j \circ I_j \Gamma_{\bullet j} \in \mathbb{R}^{N_t \times N_{el}}. \tag{33}$$

The authors of [41] propose to decompose the computation of $K\Gamma$ as $K\Gamma = D(H\Gamma)$, and based on that, proceed with the solution to the discretized reconstruction problem via ℓ_p-norm minimization [26], [41], [51], [52], [53], [54], [55]. Given that the discretized PSF operator is a tensor, we need to introduce the reshaping operator $R: \mathbb{R}^{N_x \times N_z} \mapsto \mathbb{R}^{N_x N_z}$, such that $\Gamma^* = R\Gamma \in \mathbb{R}^{N_x N_z}$. Consequently, the optimization problem at hand can now be formulated as follows:

$$\hat{\Gamma}^* = \arg\min_{\Gamma^*} \lambda \left|\left|\Gamma^*\right|\right|_p^p + \frac{1}{2}\left|\left|\tilde{G} - \tilde{K}\Gamma^*\right|\right|_2^2, \tag{34}$$

where $\tilde{K} = RKR^\dagger \in \mathbb{R}^{N_x N_z \times N_x N_z}$ represents the discretized PSF operator, λ is a regularization parameter, p is a real number such that $1 \leq p \leq 2$, and $\tilde{G} = RG \in \mathbb{R}^{N_x N_z}$ [41]. To solve this problem, the paper [41] proposes to use the fast iterative shrinkage-thresholding algorithm (FISTA) that was originally described in [56].

Chapter 3: Considered Deconvolution Settings and Evaluation Cases

3.1. Deconvolution Settings

As mentioned in Section 1.5, our main goal is to achieve the image quality level comparable to [41] at a low computational cost by adapting the BD-RPCA algorithm. With this in mind, we took several steps to make the BD-RPCA algorithm work with 2D beamformed RF data.

First, we replaced the Casorati matrix $S \in \mathbb{C}^{N_z N_x \times N_t}$ that describes a sequence of images with a single beamformed RF data frame denoted by M, and modeled in the following way:

$$M = X + L + N, \tag{35}$$

where X is a sparse component and our reconstruction target, L is a low-rank component, and N is a noise component. All these matrices belong to the set $\mathbb{R}^{N_z \times N_x}$.

Second, we decided not to separate the sparse and low-rank components during PSF estimation. This means that we no longer use RPCA in the initialization step of Algorithm 1. Instead, we rely on PSF estimation using the method described in [45] and mentioned in the previous chapter.

Next, we found that Algorithm 1 needed only one iteration to produce good-quality deconvolved images. Any subsequent iterations did not increase the performance substantially or even resulted in some artifacts. Furthermore, by limiting the algorithm to only one iteration we were able to decrease the computational cost by four times. In the next chapter, we provide an example illustrating the difference between single- and multiple-iteration execution scenarios.

Lastly, it was important to find appropriate values for hyperparameters λ, ρ, and μ

that would work well in our case. To recall, λ and ρ are the parameters that balance the relative weight of the sparse and low-rank components, respectively, while μ is another parameter that determines the convergence rate of the BD-RPCA algorithm. As the starting point, it was decided to follow the guidelines from [42] with hyperparameters' reference values of

$$\lambda_{ref} = \frac{1}{\sqrt{\max(N_z \cdot N_x, N_t)}},$$
$$\mu_{ref} = 10\lambda_{ref}, \tag{36}$$
$$\rho = 1.$$

However, since these values were suggested for the case of 3D Doppler data deconvolution, they did not work well and had to be adjusted to fit our case of 2D beamformed data deconvolution. The recommended values for the hyperparameters were found by trial-and-error, as discussed in Section 4.4.

3.2. Evaluation Cases

The next chapter presents our computational experiments that utilize two datasets from [41], corresponding to the PICMUS simulated phantom [57] and the *in vivo* carotid artery, shown in Figure 3.1. These datasets were obtained by employing the simulated and experimental probes whose characteristics are given in Table 3.1. In order to analyze the resulting B-mode images in sufficient detail, we use the dynamic range of 60 dB for the simulated phantom and 50 dB for the carotid artery.

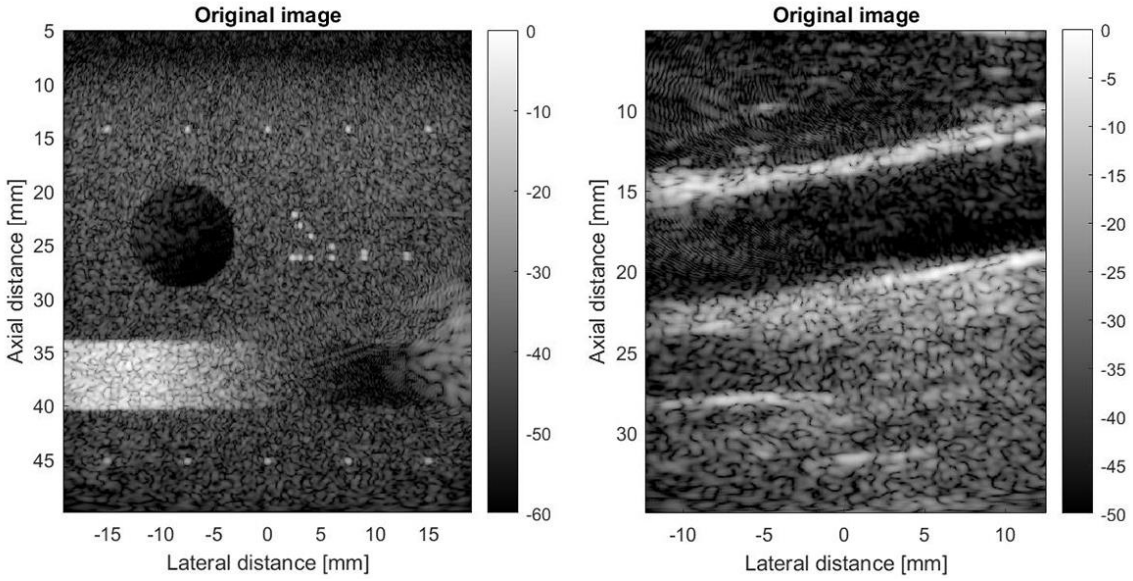

a) b)

Figure 3.1. Original B-mode images of the simulated phantom

(a) and the carotid artery (b) before deconvolution.

Table 3.1. Probe characteristics [41].

	Simulated probe: L11-4v [58]	Experimental probe: L12-5 50mm [59]
Element number	128	128
Excitation	Plane wave	Plane wave
Center frequency	5.133 MHz	7.8 MHz
Sampling frequency	20.832 MHz	31.2 MHz
Element width	270 μm	Unknown
Pitch	300 μm	195 μm
Elevation focus	20 mm	Unknown

We have considered the following four evaluation cases:

- **Case 1.** Deconvolution involves applying the FISTA algorithm to solve the ℓ_p-norm minimization problem (34), where the stationary PSF is fixed and given in advance. In other words, this is the case of non-blind deconvolution.

- **Case 2.** Deconvolution is based on solving the ℓ_p-norm minimization problem, but the stationary PSF is now estimated from the given beamformed RF data.
- **Case 3.** Deconvolution involves applying the adapted BD-RPCA algorithm, where the stationary PSF is estimated from the given beamformed RF data.
- **Case 4.** Deconvolution is based on solving the ℓ_p-norm minimization problem, while using the non-stationary PSF obtained from the given beamformed RF data.

The first case uses the prestored stationary PSF that was obtained in [41] from previous Field-II simulations [58]. Those simulations involved a synthetic single-scatterer phantom positioned at the 25-mm depth [41]. The second and the third cases use the stationary PSF that was estimated from the available beamformed RF data using the method proposed by O. Michailovich and D. Adam in [45]. The fourth case represents the experiments evaluating the use of the estimated non-stationary PSF operator [41].

Figure 3.2 shows the PSFs that were used in our computational experiments. As described earlier, the prestored simulated PSF was used in case 1, while the estimated (stationary) PSF was used in cases 2 and 3. Unfortunately, the PSF for case 4 is difficult to visualize, since it is represented by a complicated non-stationary operator. As it can be seen, different cases involve different PSFs coupled with different methods for deconvolution. However, despite such differences, all of them provide a significant improvement over the original low-resolution images.

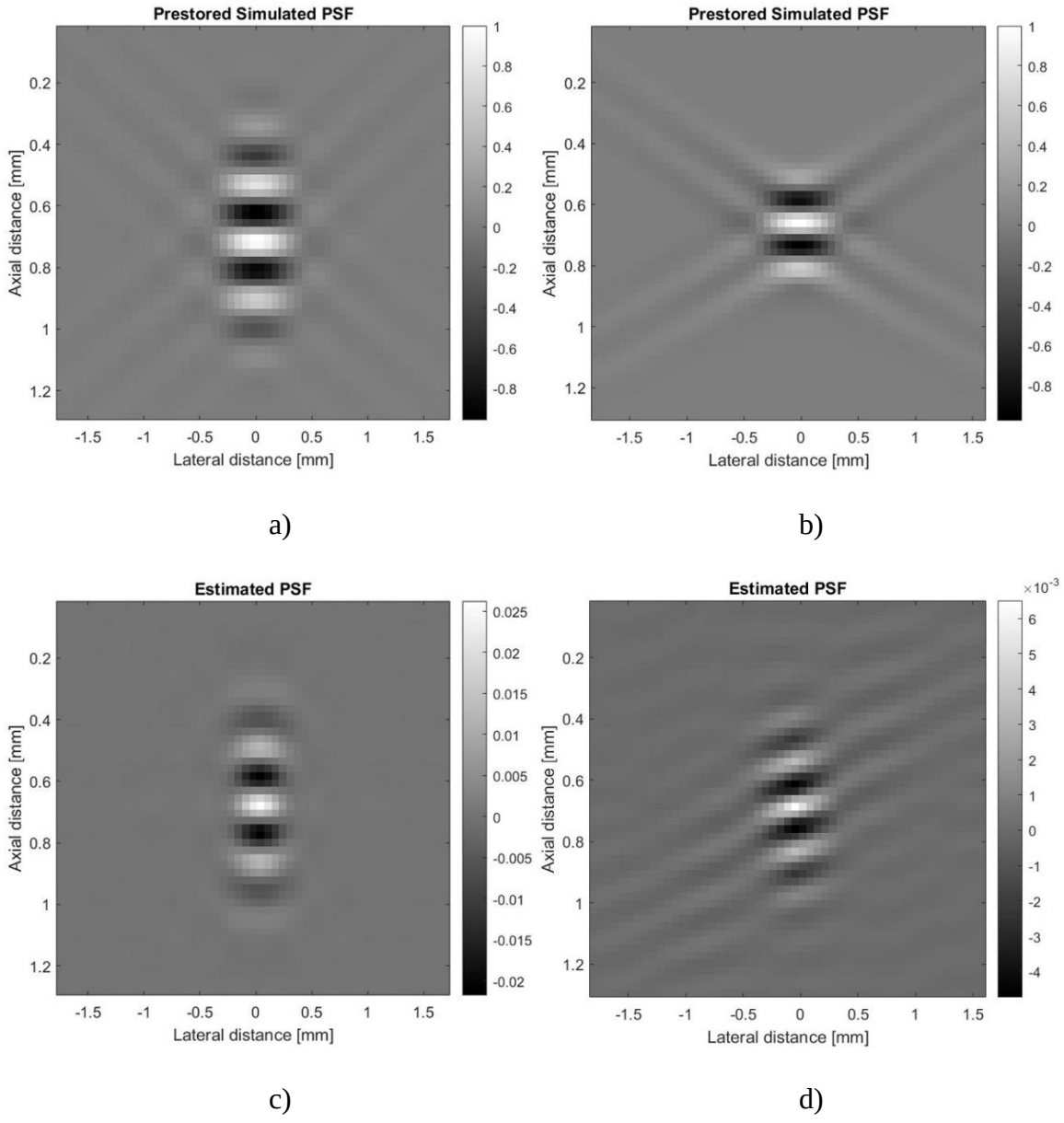

Figure 3.2. Prestored simulated PSFs used for PICMUS (a) and artery (b) RF data deconvolution. Estimated PSFs for PICMUS (c) and artery (d) RF data deconvolution.

As mentioned previously, our computational experiments employ two different deconvolution approaches: either solving the ℓ_p-norm minimization problem (34), or solving the BD-RPCA problem (12). For their respective cases, we also explore multiple subcases representing various settings of the corresponding user-controlled hyperparameters. When dealing with the ℓ_p-norm minimization problem, we considered

$p = 1.25, 1.50, 1.75$. When dealing with the BD-RPCA problem, we considered $\lambda = 0.0375, 0.375, 3.75$, $\rho = 0.05, 0.5, 5$, and $\mu = 10^{-10}, 10^{-6}, 10^{-2}$ for the simulated phantom dataset, and $\lambda = 0.00003, 0.0003, 0.003$, $\rho = 0.05, 1, 20$, and $\mu = 10^{-12}, 10^{-8}, 10^{-4}$ for the carotid artery dataset. All these subcases are discussed in Chapter 4 presenting our evaluation results.

Chapter 4: Evaluation Results

4.1. Evaluation Metrics

Our evaluation metrics are as follows: the contrast-to-noise ratio (CNR) and lateral/axial full width at half maximum (FWHM) for the PICMUS simulated phantom, as well as the structural similarity index measure (SSIM), peak signal-to-noise ratio (PSNR), signal-to-noise ratio (SNR), and tissue-to-clutter ratio (TCR) for the carotid artery. Because there are no ground-truth images for the *in vivo* carotid artery, the original B-mode image before deconvolution is used as the reference. Consequently, SSIM and PSNR will indicate how much of a change the deconvolution algorithms introduced.

The CNR [60] is a measure of the contrast between the tissue and the background, calculated on the normalized envelope image as

$$CNR = 20\log_{10}\frac{|\mu_t - \mu_b|}{\sqrt{\frac{\sigma_b^2 + \sigma_t^2}{2}}}, \tag{37}$$

where μ_t, μ_b and σ_t^2, σ_b^2 are the mean values and the variances of the target inclusion (the anechoic region in Figure 3.1 (a)) and the background around it, respectively [41].

Lateral and axial resolution for point-like targets is quantified by the FWHM values computed on the log-compressed B-mode images [41], [60]. We report the FWHM averages for the two groups of points located at 14 mm and 45 mm shown in Figure 3.1 (a).

The SSIM measures the similarity between two digital images x and y. Its formula can be written as follows:

$$SSIM(x,y) = \frac{(2\mu_x\mu_y + c_1)(2\sigma_{xy} + c_2)}{(\mu_x^2 + \mu_y^2 + c_1)(\sigma_x^2 + \sigma_y^2 + c_2)} \tag{38}$$

where μ_x and μ_y are the average of x and y, respectively, σ_x^2 and σ_y^2 are the variance of x and y, respectively, σ_{xy} is a covariance of x and y, $c_1 = (k_1 L)^2, c_2 = (k_2 L)^2$ are two variables introduced to stabilize the division, with L being the dynamic range of the pixel-values, $k_1 = 0.01$, and $k_2 = 0.03$.

The PSNR is the ratio between the maximum pixel value squared and the power of noise represented by the mean squared error (MSE):

$$PSNR = 10 \log_{10} \left(\frac{d_{max}^2}{MSE} \right), \tag{39}$$

where $MSE = \frac{1}{N_z N_x} \left| |Ref - I| \right|_F^2$, d_{max} denotes the maximum pixel value, N_z and N_x symbolize the size of the images, I represents the observed image, and Ref denotes reference image.

The TCR is the ratio between the average pixel intensity in tissue and background regions [41]

$$TCR = 20 \log_{10} \left(\frac{\mu_t}{\mu_b} \right), \tag{40}$$

where μ_t and μ_b are mean pixel values of tissue and background regions, respectively. Both mean values are found on the normalized envelope of the beamformed RF data. Similarly, the SNR is the ratio between the power of the image and the power of the noise. It is given by

$$SNR = \frac{|\mu_t - \mu_b|}{\sqrt{\sigma_b^2 + \sigma_t^2}}, \tag{41}$$

where σ_t and σ_b are the standard deviation of the pixel intensities in tissue and background regions, respectively. Mean values and standard deviations are found after logarithmic compression of the normalized envelope. In order to calculate SNR and TCR, we use three regions of interest, highlighted in Figure 4.1, where background regions 1 and 2 are located inside the carotid artery, while tissue region 3 is outside the artery.

To estimate the average deconvolution time of all algorithms, their respective MATLAB 2019b scripts were executed 10 times on a Windows 10 computer equipped with 16 GB RAM and Intel Core i7-8550U CPU running at 1.80 GHz. Note, the reported running times include only the deconvolution process, excluding the time spent for the PSF estimation. The latter takes approximately 108 seconds on average, when using the method proposed in [45].

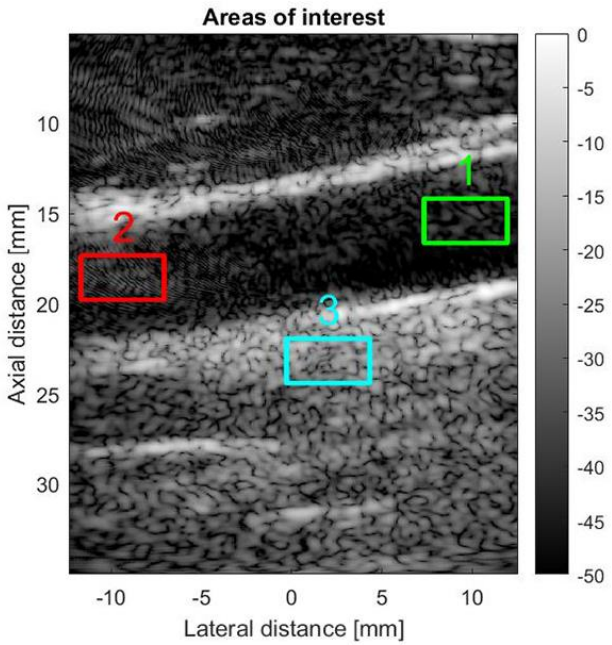

Figure 4.1. Background (1 and 2) and tissue (3) regions used for SNR and TCR calculations.

4.2. Case 1: Deconvolution Using Prestored Simulated PSF

As mentioned in the previous chapter, in this case, deconvolution involves applying the FISTA algorithm to solve the ℓ_p-norm minimization problem (34), where the stationary PSF was obtained from Field-II simulations and prestored in advance.

PICMUS Phantom. The resulting images of the PICMUS simulated phantom after deconvolution can be seen in Figure 4.2, with the evaluation metrics presented in Table 4.1.

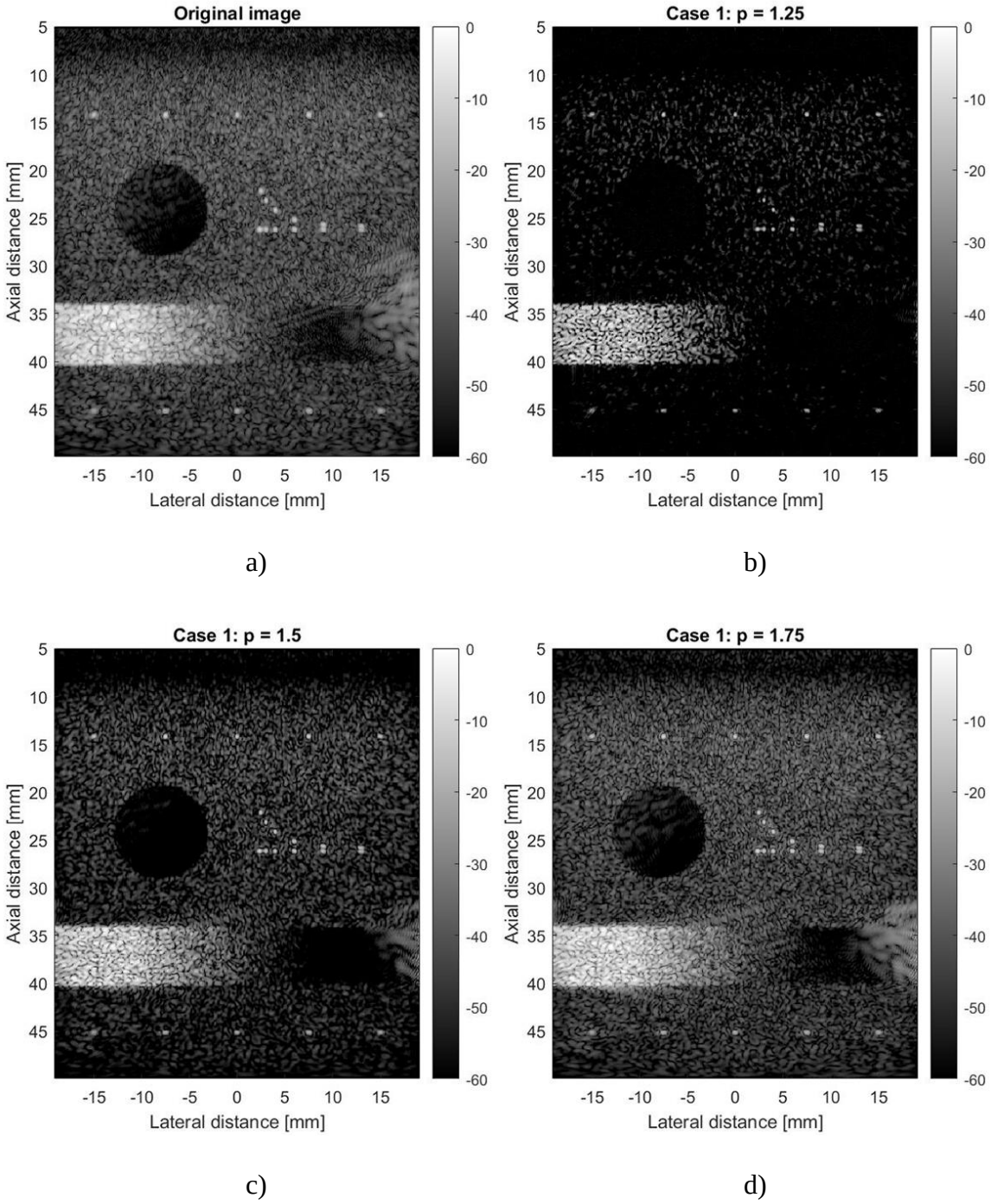

Figure 4.2. B-mode images of the simulated phantom before (a) and after deconvolution using the prestored PSF with $p = 1.25$ (b), $p = 1.5$ (c), $p = 1.75$ (d).

Table 4.1 shows that the best results in terms of the resolution are achieved when the value of p approaches one. This can be explained by the fact that the values of p that are close to one promote sparse components of the image, such as bright "spikes" created

by hyperechoic point-like targets. On the other hand, prioritizing sparsity can cause a decrease in the CNR value. In the subcase with $p = 1.25$, CNR turns out to be negative. On the contrary, the subcase with $p = 1.75$ leads to a better result in terms of CNR but worsens the FWHM values. However, choosing the value of p too high can also lead to a lower CNR. Based on these observations, it is important to find the value of p that would improve the resolution of the image while maintaining high CNR. In this case, the setting of $p = 1.5$ provided an appreciable improvement in both FWHM and CNR in comparison with the original image. In terms of computational complexity, the subcase with $p = 1.25$ was the worst taking 1311.92 seconds, while the subcase with $p = 1.5$ had the lowest computational cost of 21.92 seconds. Taking all of the above into consideration, we recommend the value of $p = 1.5$.

Table 4.1. Image quality indicators for simulated phantom, Case 1.

	CNR, dB	**Lateral resolution, mm**		**Axial resolution, mm**		**Time, s**
		14 mm	**45 mm**	**14 mm**	**45 mm**	
a) Original image	6.6	0.36	0.53	0.38	0.41	–
b) Case 1, $p = 1.25$	-12.3	**0.27**	**0.29**	**0.21**	**0.19**	1311.92
c) Case 1, $p = 1.5$	**7**	0.30	0.41	0.27	0.26	**21.92**
d) Case 1, $p = 1.75$	5.5	0.34	0.47	0.31	0.31	41.51

Carotid Artery. The resulting images of the carotid artery after deconvolution can be seen in Figure 4.3, with the evaluation metrics presented in Table 4.2. Figure 4.3 shows that all three subcases with different values of p were able to improve the overall quality of the image: the images look sharper and the blur is reduced. After deconvolution with $p = 1.25, 1.5, 1.75$, the images have the SSIM values of 0.7661, 0.8022, and 0.8834, respectively. In the subcase with $p = 1.25$, the algorithm introduced

the greatest amount of change, however, it is easy to notice that this change is not entirely positive in terms of the SNR values. Furthermore, the computation time of this subcase is more than 100 times and 72 times slower compared to the subcases with $p = 1.5$ and $p = 1.75$, respectively.

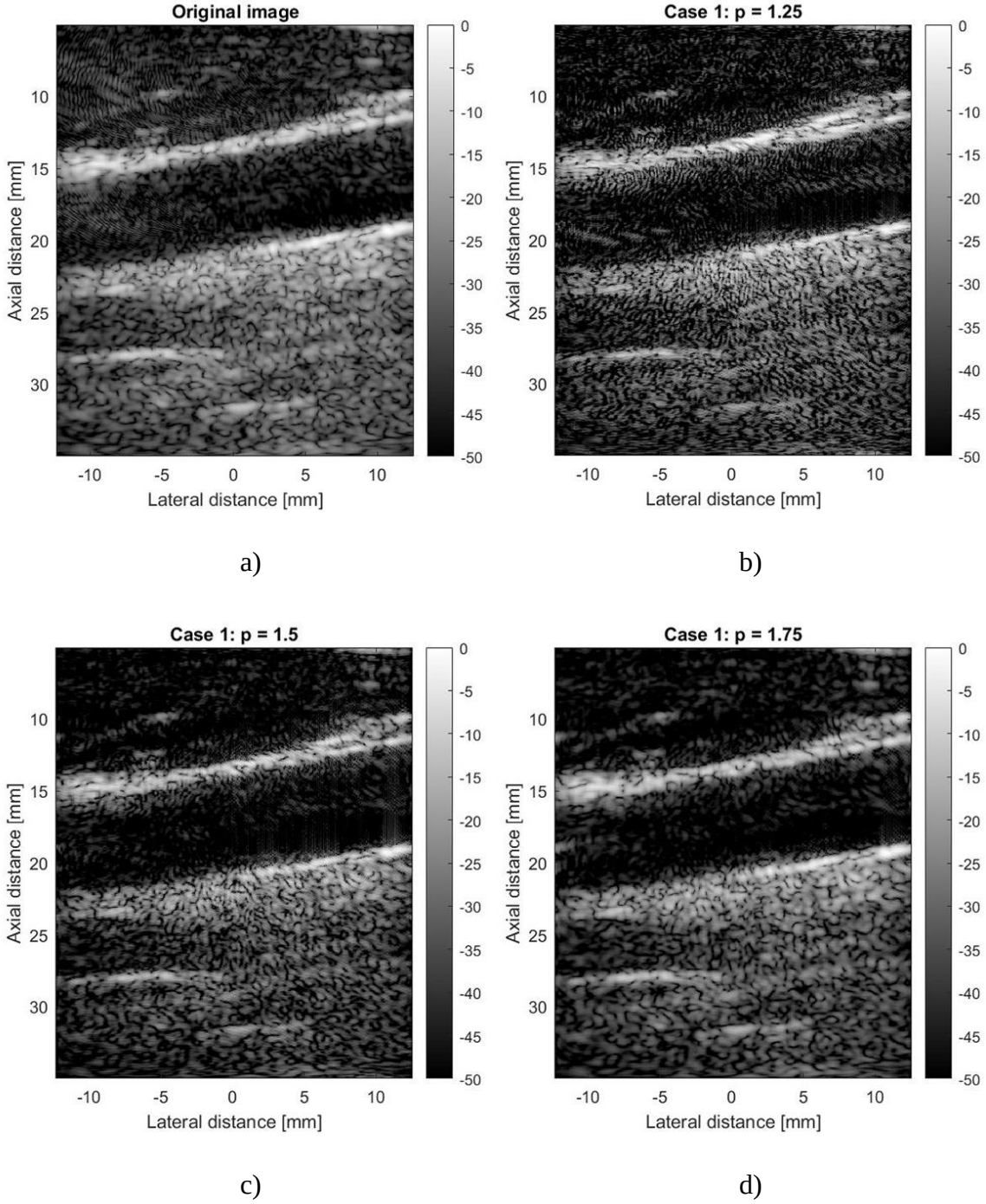

Figure 4.3. B-mode images of the carotid artery before (a) and after deconvolution using the prestored PSF with $p = 1.25$ (b), $p = 1.5$ (c), $p = 1.75$ (d).

As one can see, the carotid artery images exhibit the same pattern as the PICMUS phantom images: the low value of p promotes "spikes", while high values of p promote smoothness or low variance. This behavior can be observed in the SNR of the images – the lower value of p leads to a lower SNR caused by higher variance. In terms of TCR, the second region of the artery shows some significant improvement in all three subcases, while the first region was only improved in the subcase of $p = 1.75$. However, the subcase with $p = 1.5$ performed better than the subcase with $p = 1.75$ in the second region. If we calculate the average TCR of both regions, both subcases with $p = 1.5$ and $p = 1.75$ yield approximately the same value. As for the average SNR, the subcase with $p = 1.75$ outperforms the subcase with $p = 1.5$, and the former is the only subcase that improved the SNR values of both regions compared to the original image. Given all of the above, the subcase with $p = 1.75$ is arguably better than the other two subcases and, therefore, is recommended.

Table 4.2. Image quality indicators for carotid artery, Case 1.

	SSIM	**PSNR, dB**	**SNR – 1st region**	**SNR – 2nd region**	**TCR – 1st region, dB**	**TCR – 2nd region, dB**	**Time, s**
a) Original image	Ref.	Ref.	**42.523**	40.651	20.781	17.554	–
b) Case 1, $p = 1.25$	0.7661	26.744	32.157	32.523	19.298	20.397	1308.51
c) Case 1, $p = 1.5$	0.8022	28.99	39.599	40.085	19.652	**20.839**	**12.34**
d) Case 1, $p = 1.75$	0.8834	33.051	42.188	**41.333**	**21.34**	19.47	18.02

4.3. Case 2: Deconvolution Using Estimated Stationary PSF

This case focuses on blind deconvolution using the stationary PSF that is estimated from the given beamformed RF data.

PICMUS Phantom. Figure 4.4 shows the resulting images of the PICMUS simulated phantom after deconvolution. The corresponding evaluation metrics can be found in Table 4.3.

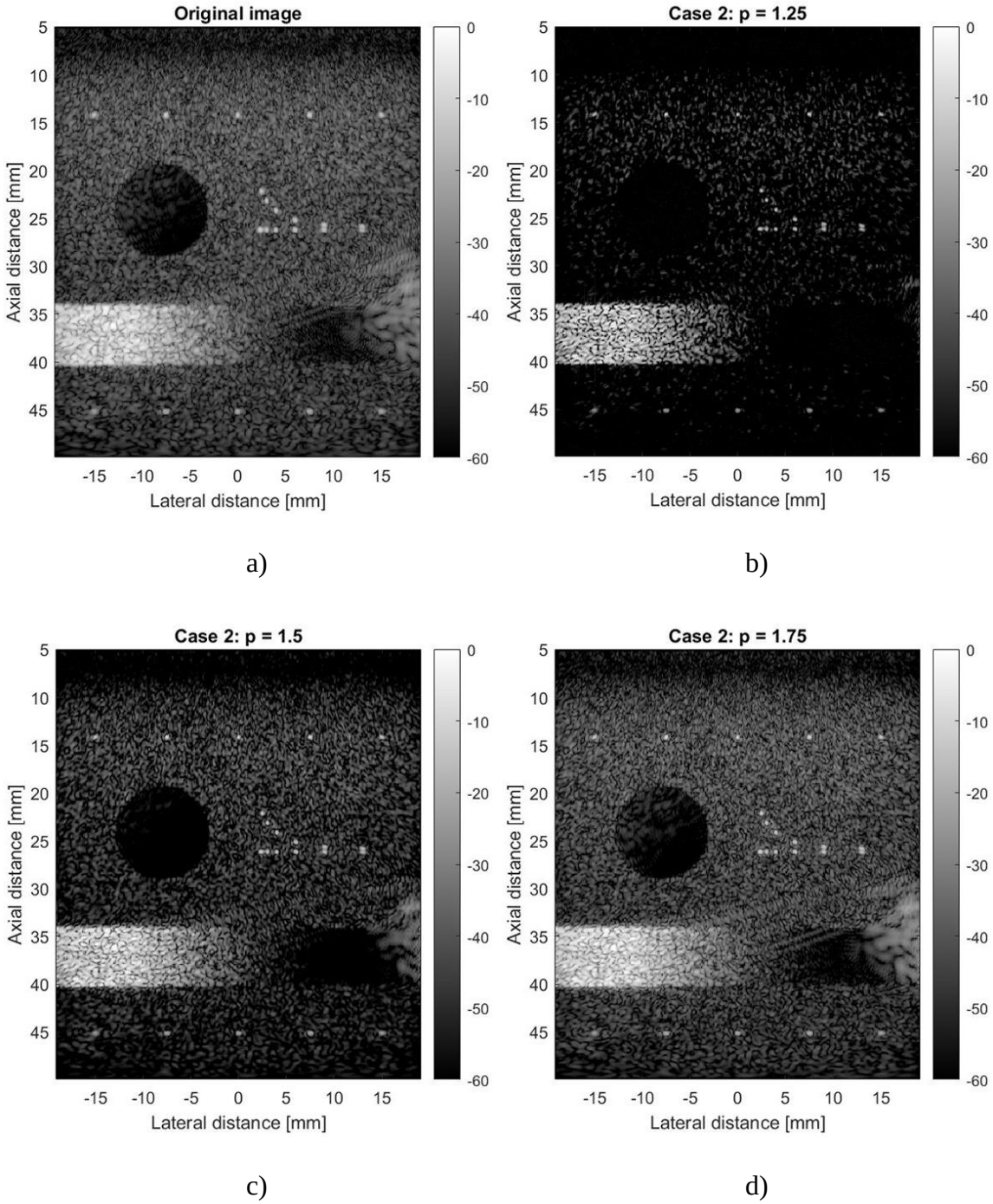

Figure 4.4. B-mode images of the simulated phantom before (a) and after deconvolution using the estimated PSF with $p = 1.25$ (b), $p = 1.5$ (c), $p = 1.75$ (d).

Based on these results, the same trend as in case 1 is observed: the low value of p prioritizes "spikes" in the signal, which leads to better FWHM but worse CNR values, while higher values of p result in higher CNR but lower FWHM values. The subcase with $p = 1.5$ offers a good balance between high resolution and high contrast, while taking the least amount of time to perform deconvolution. For this reason, the value of $p = 1.5$ is recommended for this case.

Table 4.3. Image quality indicators for simulated phantom, Case 2.

	CNR, dB	**Lateral resolution, mm**		**Axial resolution, mm**		**Time, s**
		14 mm	**45 mm**	**14 mm**	**45 mm**	
a) Original image	6.6	0.36	0.53	0.38	0.41	–
b) Case 2, $p = 1.25$	-8.6	**0.20**	**0.41**	**0.17**	**0.23**	1411.84
c) Case 2, $p = 1.5$	**7**	0.25	0.47	0.23	0.30	**21.19**
d) Case 2, $p = 1.75$	5.7	0.29	0.49	0.29	0.33	35.84

Carotid Artery. Figure 4.5 shows the images obtained after performing deconvolution of the carotid artery beamformed data using the estimated PSF. Image quality indicators for this case can be found in Table 4.4. As it can be seen, this approach resulted in some improvements to the SNR and TCR in the subcases with $p = 1.5$ and 1.75, respectively. However, ℓ_p-norm minimization did not work as well with $p = 1.25$, which also took a much longer time to finish deconvolution compared to the subcase with $p = 1.5$ and $p = 1.75$. Here we can notice the same pattern as we observed in Section 4.2: using small values of p tends to produce sharper images, while using larger values of p tends to produce smoother images. In terms of TCR, all three subcases increased the image quality in both regions. The subcase with $p = 1.75$ provided slightly better improvements compared to the subcase with $p = 1.5$. However, based on SNR,

computational cost, and insignificant difference in TCR in these two subcases, it is recommended to choose $p = 1.5$ for this case. This decision corresponds to the one made earlier for the PICMUS simulated phantom.

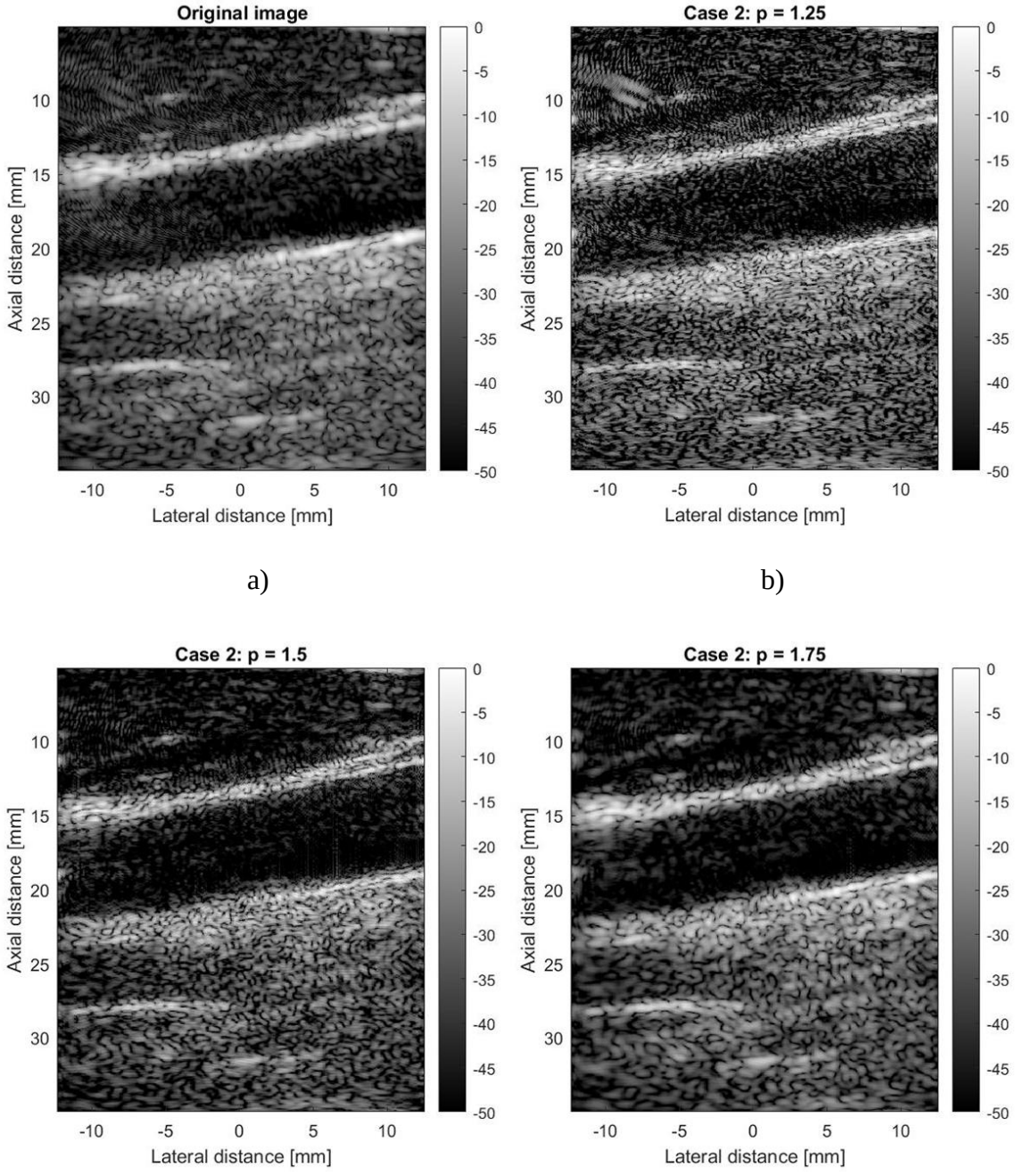

a) b)

c) d)

Figure 4.5. B-mode images of the carotid artery before (a) and after deconvolution using the estimated PSF with $p = 1.25$ (b), $p = 1.5$ (c), $p = 1.75$ (d).

Table 4.4. Image quality indicators for carotid artery, Case 2.

	SSIM	PSNR, dB	SNR – 1st region	SNR – 2nd region	TCR – 1st region, dB	TCR – 2nd region, dB	Time, s
a) Original image	Ref.	Ref.	42.523	40.651	20.781	17.554	–
b) Case 2, $p = 1.25$	0.7678	26.976	41.449	39.308	21.893	17.901	1318.69
c) Case 2, $p = 1.5$	0.8599	29.328	**42.808**	**41.952**	22.016	20.201	**12.53**
d) Case 2, $p = 1.75$	0.9349	35.278	35.613	34.969	**22.408**	**20.529**	23.41

4.4. Case 3: Deconvolution Using Estimated Stationary PSF and RPCA

This case provides the deconvolution results for the adapted BD-RPCA algorithm with the use of the estimated PSF. To produce acceptable images, it was important to tune the hyperparameters as mentioned in Section 3.2.

PICMUS Phantom. The resulting images of the PICMUS simulated phantom after deconvolution are shown in Figure 4.6, with the evaluation metrics presented in Table 4.5. As it can be seen, different hyperparameters can affect the BD-RPCA algorithm differently. Recall that the hyperparameters λ and ρ essentially change the relative contribution of the sparse and low-rank components to the optimization objective function, thus balancing out the tradeoff between them. When we increase the value of λ, we promote image sparsity. On the other hand, higher values of ρ promote low-rankness, which allows to include more details (also carrying the noise) in the final image. Lastly, the hyperparameter μ determines the convergence rate of the algorithm that affects its computational cost.

Overall, the adapted BD-RPCA yields resolution improvements at a low computational cost compared to the previous two cases, however, the CNR values are substantially worse. Such a result can be explained by the fact that the sparse component is our reconstruction target that is being deconvolved. Based on the evaluation metrics

presented in Table 4.5, the hyperparameters $\lambda = 0.375, \rho = 0.5, \mu = 10^{-6}$ are recommended for use in this particular case providing improved FWHM and bearable CNR values.

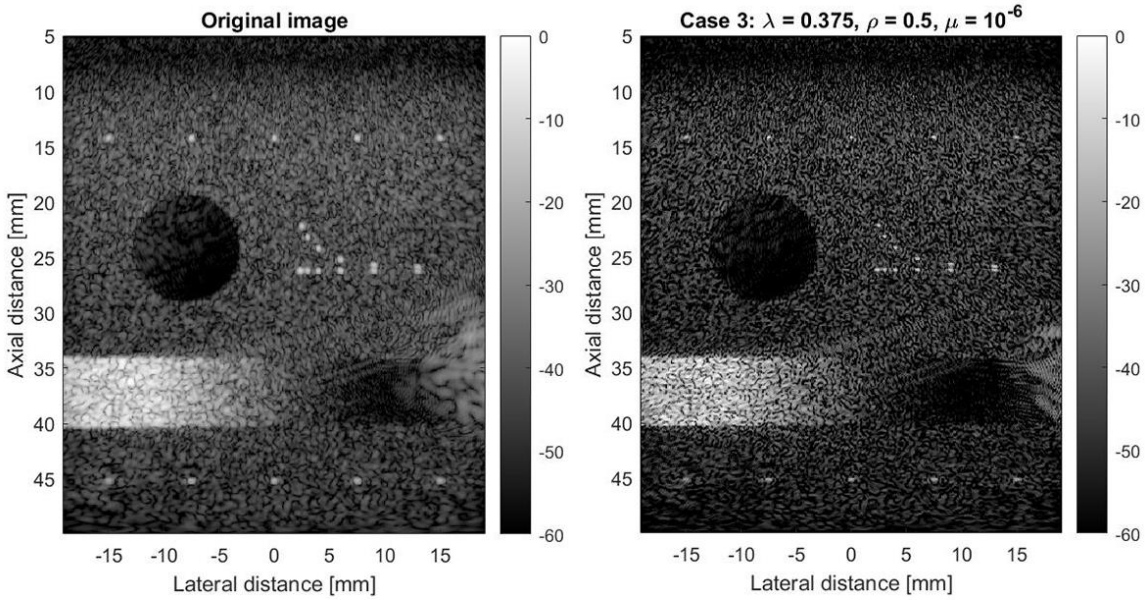

a)

b)

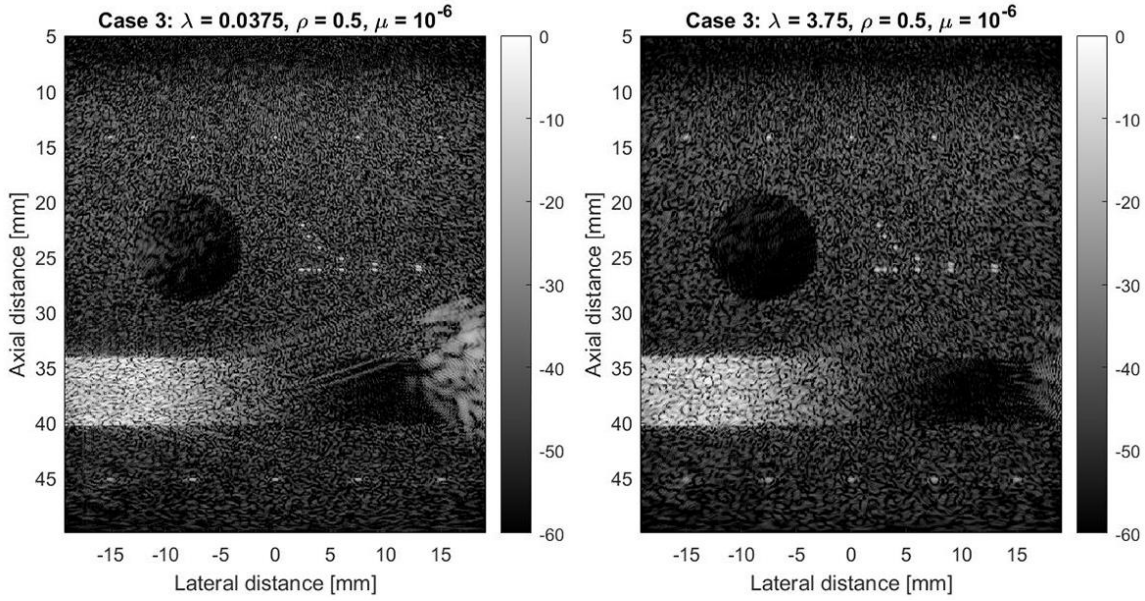

c)

d)

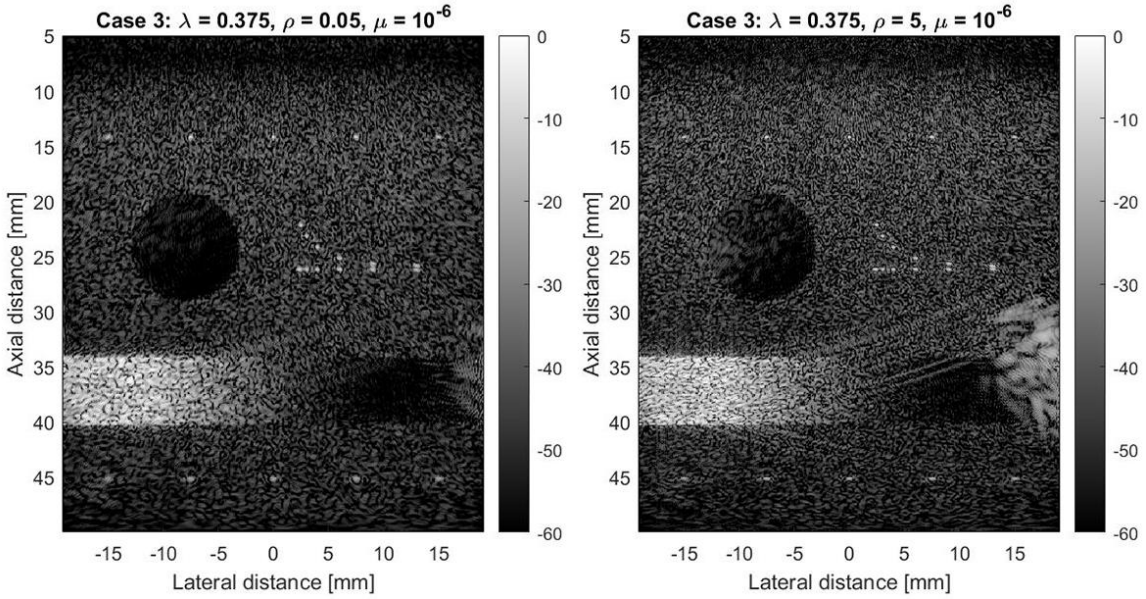

e) f)

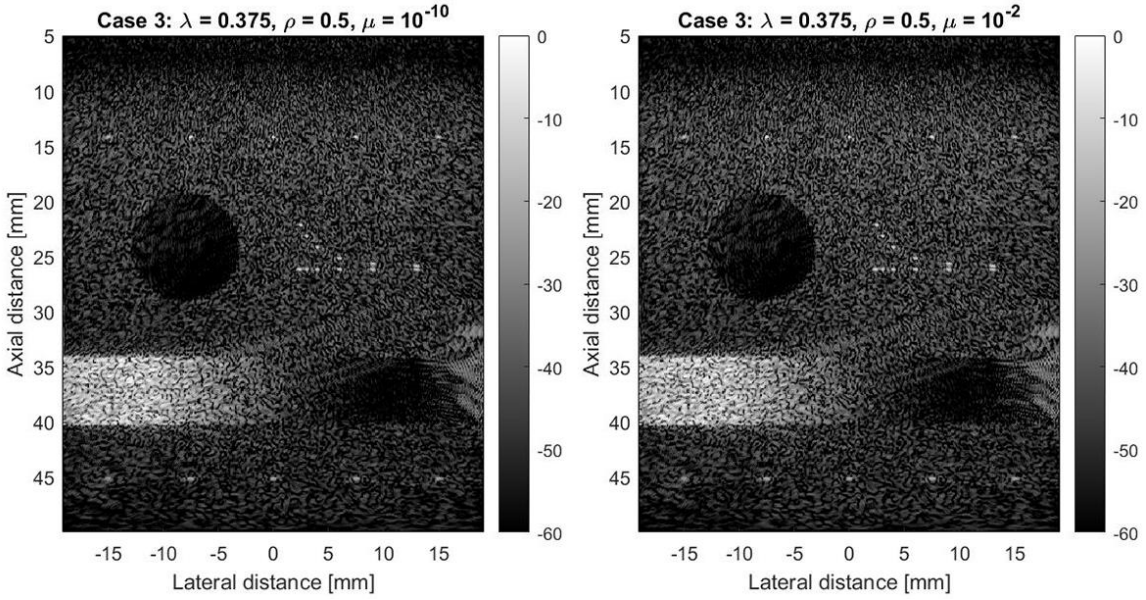

g) h)

Figure 4.6. B-mode images of the simulated phantom before (a) and after deconvolution using the estimated PSF and RPCA algorithm with $\lambda = 0.375, \rho = 0.5, \mu = 10^{-6}$ (b), $\lambda = 0.0375, \rho = 0.5, \mu = 10^{-6}$ (c), $\lambda = 3.75, \rho = 0.5, \mu = 10^{-6}$ (d), $\lambda = 0.375, \rho = 0.05, \mu = 10^{-6}$ (e), $\lambda = 0.375, \rho = 5, \mu = 10^{-6}$ (f), $\lambda = 0.375, \rho = 0.5, \mu = 10^{-10}$ (g), and $\lambda = 0.375, \rho = 0.5, \mu = 10^{-2}$ (h).

Table 4.5. Image quality indicators for simulated phantom, Case 3.

	CNR, dB	Lateral resolution, mm		Axial resolution, mm		Time, s
		14 mm	45 mm	14 mm	45 mm	
a) Original image	**6.6**	0.36	0.53	0.38	0.41	–
b) Case 3, $\lambda = 0.375, \rho = 0.5, \mu = 10^{-6}$	1.3	**0.20**	0.48	0.16	0.21	7.17
c) Case 3, $\lambda = 0.0375, \rho = 0.5, \mu = 10^{-6}$	-1.3	0.23	**0.47**	0.17	**0.15**	6.68
d) Case 3, $\lambda = 3.75, \rho = 0.5, \mu = 10^{-6}$	2.1	0.24	0.51	0.20	0.27	8.34
e) Case 3, $\lambda = 0.375, \rho = 0.05, \mu = 10^{-6}$	2.1	0.23	0.50	0.20	0.27	7.12
f) Case 3, $\lambda = 0.375, \rho = 5, \mu = 10^{-6}$	-1.3	0.23	**0.47**	**0.15**	0.17	7.14
g) Case 3, $\lambda = 0.375, \rho = 0.5, \mu = 10^{-10}$	1.3	**0.20**	0.48	0.16	0.21	9.13
h) Case 3, $\lambda = 0.375, \rho = 0.5, \mu = 10^{-2}$	1.1	**0.20**	0.48	0.17	0.21	**4.66**

Carotid Artery. The results of deconvolution of the carotid artery images using the adapted BD-RPCA are shown in Figure 4.7. Table 4.6 represents the evaluation metrics for this case. Unfortunately, the BD-RPCA algorithm required significant adjustments of the hyperparameters, i.e., the values of λ, ρ, and μ used for the simulated PICMUS phantom images did not work at all for the *in vivo* carotid artery images. Despite the difference in the hyperparameters, the algorithm follows the same trend, as described earlier. For example, Figure 4.7 (d) shows that by increasing λ we increased the sparse component's influence on the final result, thus eliminating a lot of image details that led to the value of SSIM being equal to 0.4993. On the other hand, a small value of λ, shown in Figure 4.7 (c), preserved most of the image details, leading to the SSIM value of 0.9068. A reversed pattern can be seen with respect to ρ: smaller values of ρ tend to filter out the image details to a larger extent (e.g., see Figure 4.7 (e) vs. (f)). These observations

are reflected in the SSIM values as well: the small value of ρ gives SSIM = 0.4819, while the high value of ρ gives SSIM = 0.8969.

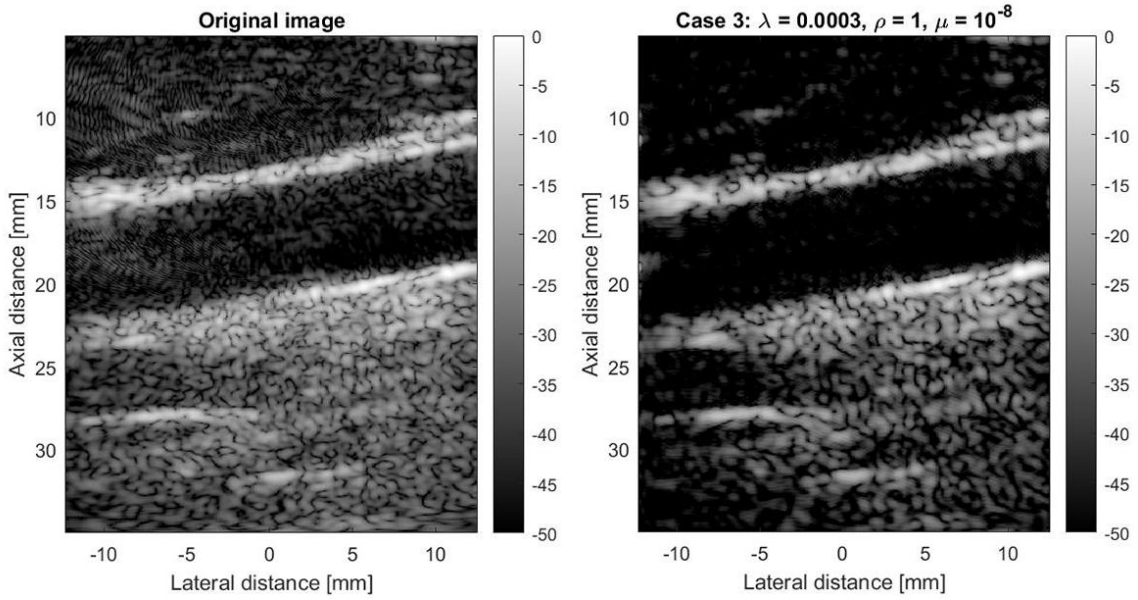

a)

b)

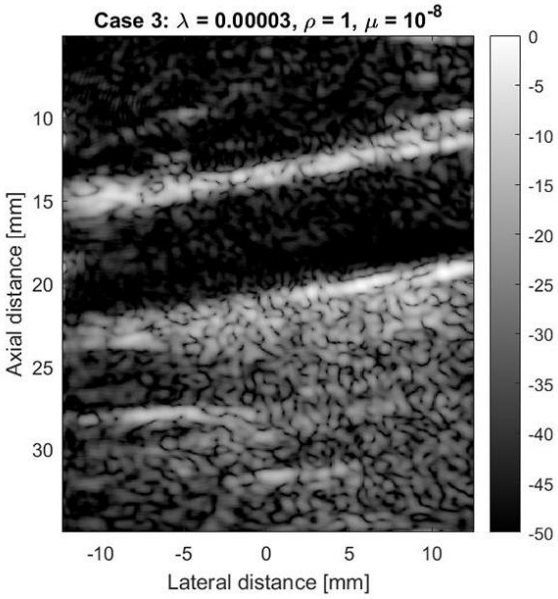

c)

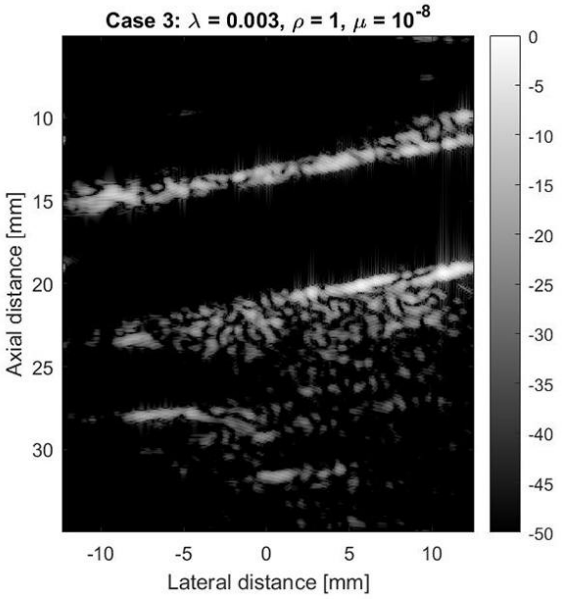

d)

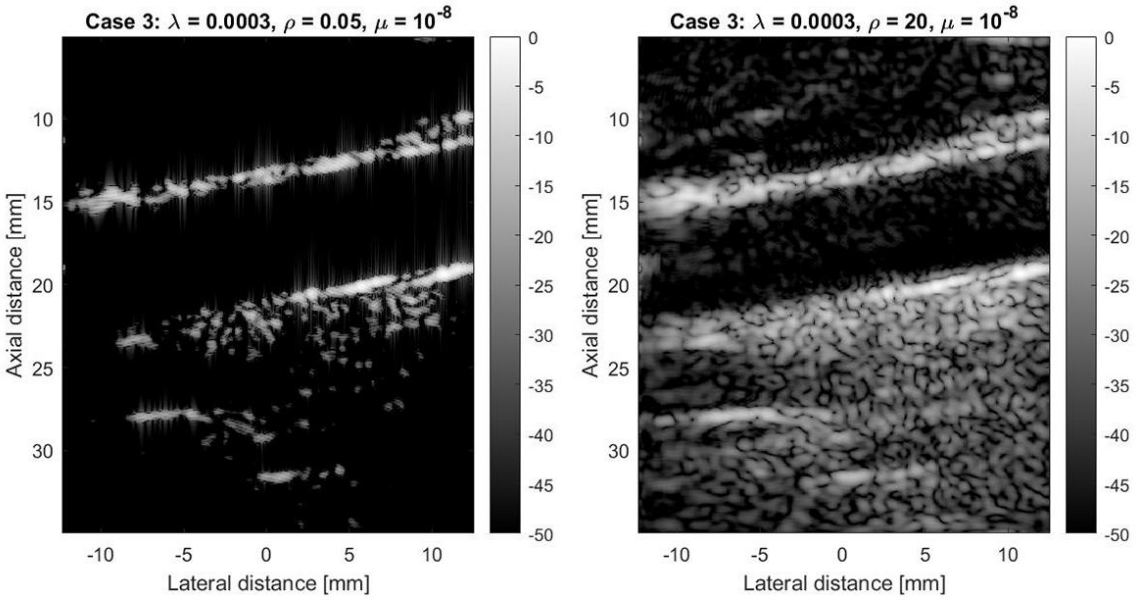

e) f)

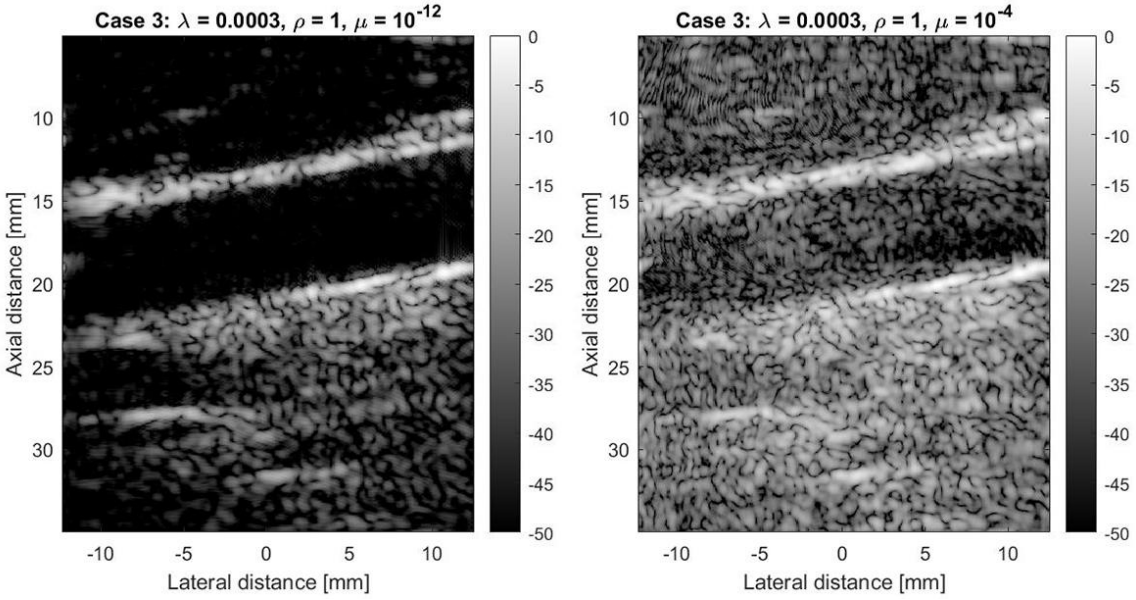

g) h)

Figure 4.7. B-mode images of the carotid artery before (a) and after deconvolution using the estimated PSF and RPCA algorithm with $\lambda = 0.0003, \rho = 1, \mu = 10^{-8}$ (b), $\lambda = 0.00003, \rho = 1, \mu = 10^{-8}$ (c), $\lambda = 0.003, \rho = 1, \mu = 10^{-8}$ (d), $\lambda = 0.0003, \rho = 0.05, \mu = 10^{-8}$ (e), $\lambda = 0.0003, \rho = 20, \mu = 10^{-8}$ (f), $\lambda = 0.0003, \rho = 1, \mu = 10^{-12}$ (g), and $\lambda = 0.0003, \rho = 1, \mu = 10^{-4}$ (h).

As mentioned earlier, the value of μ is responsible for the convergence rate of the algorithm. Figure 4.7 (h) shows that the high value of μ can lead to very poor visual outcomes. The deconvolution result for the small value of μ is depicted in Figure 4.7 (g). One can notice that Figure 4.7 (b) and Figure 4.7 (g) are very similar and the evaluation metrics confirm this observation. Furthermore, if we measure the similarity index between these two images, we get SSIM = 0.992. In other words, after a certain value of μ, the quality of the deconvolved image does not improve significantly no matter how small μ becomes. Besides that, the smaller the convergence rate the higher the computational cost, as illustrated in Table 4.6.

Table 4.6. Image quality indicators for carotid artery, Case 3.

	SSIM	**PSNR, dB**	**SNR – 1st region**	**SNR – 2nd region**	**TCR – 1st region, dB**	**TCR – 2nd region, dB**	**Time, s**
a) Original image	Ref.	Ref.	**42.523**	**40.651**	20.781	17.554	–
b) Case 3, $\lambda = 0.0003, \rho = 1, \mu = 10^{-8}$	0.7695	32.652	32.489	32.17	**26.621**	25.576	3.42
c) Case 3, $\lambda = 0.00003, \rho = 1, \mu = 10^{-8}$	0.9068	36.243	38.894	38.068	22.962	20.522	3.38
d) Case 3, $\lambda = 0.003, \rho = 1, \mu = 10^{-8}$	0.4993	27.138	22.148	22.303	20.723	**25.696**	3.56
e) Case 3, $\lambda = 0.0003, \rho = 0.05, \mu = 10^{-8}$	0.4819	26.869	12.182	12.312	16.875	21.591	2.78
f) Case 3, $\lambda = 0.0003, \rho = 20, \mu = 10^{-8}$	0.8969	36.139	36.389	35.525	22.936	20.292	4.17
g) Case 3, $\lambda = 0.0003, \rho = 1, \mu = 10^{-12}$	0.7291	31.036	35.301	34.996	25.496	25.323	5.54
h) Case 3, $\lambda = 0.0003, \rho = 1, \mu = 10^{-4}$	0.6553	26.362	34.165	34.019	16.692	16.53	**1.34**

Based on the SNR and TCR metrics, we highlight two subcases shown in Figure 4.7 (b) and (c). The first subcase does a better job in terms of TCR by emphasizing sparsity, while the second subcase wins in terms of SNR by promoting low-rankness of the image. These two subcases will be compared to the others in Section 4.6.

As it was mentioned in Section 3.1, we introduced some minor changes to the original BD-RPCA algorithm. For example, we are limiting Algorithm 1 to only one iteration to decrease the computational cost. The results of the deconvolution with and without this change are shown in Figure 4.8. As we can see from Table 4.7, the algorithm did not produce any noticeable improvements past the first iteration. This is confirmed by the SSIM value of 0.997 between them. Furthermore, if we compare the other image evaluation metrics, provided in Table 4.7, we can observe that all of them are very similar. It is also important to mention that multiple iterations not only fail to provide appreciable image quality improvements, but also increase the computational cost by four times.

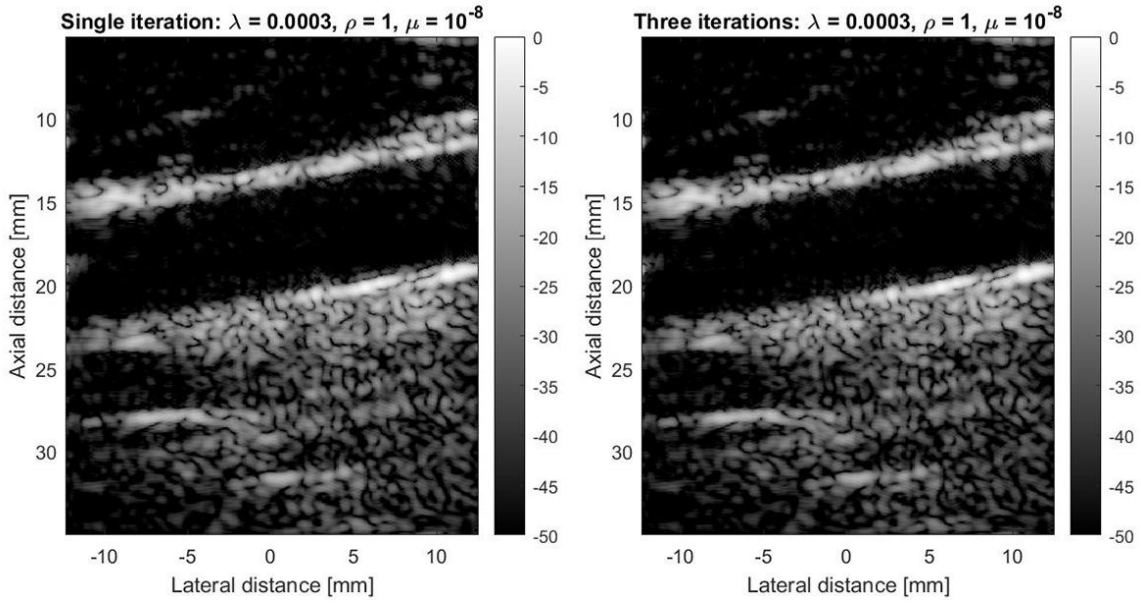

a) b)

Figure 4.8. B-mode images of the carotid artery after deconvolution using one (a) and three (b) iterations of the BD-RPCA algorithm.

Table 4.7. Image quality indicators for a single- and three-iteration execution of BD-RPCA.

	SSIM	PSNR, dB	SNR – 1st region	SNR – 2nd region	TCR – 1st region, dB	TCR – 2nd region, dB	Time, s
a) Single iteration BD-RPCA	0.7695	32.652	32.489	32.17	26.621	25.576	3.42
b) Three iterations BD-RPCA	0.7641	32.205	32.5	32.348	26.179	25.842	14.26

4.5. Case 4: Deconvolution Using Estimated Non-stationary PSF

This case describes deconvolution that is based on solving the ℓ_p-norm minimization problem, while using the non-stationary PSF obtained from the given beamformed RF data.

PICMUS Phantom. Figure 4.9 shows the resulting images of the PICMUS simulated phantom after deconvolution, with the corresponding evaluation metrics presented in Table 4.8. It can be seen that the subcase with $p = 1.25$ has introduced some noticeable artifacts, worsened the CNR, and run for the longest amount of time. The subcase with $p = 1.75$ has the best performance in terms of CNR but is outperformed by the other two subcases in terms of FWHM. Lastly, the subcase with $p = 1.5$ is able to achieve a significant enhancement in resolution surpassing the other two subcases, while achieving the CNR value of only 0.1 dB less than that in the subcase with $p = 1.75$. Based on this observation and computational cost, the value of $p = 1.5$ is recommended for this case of deconvolution.

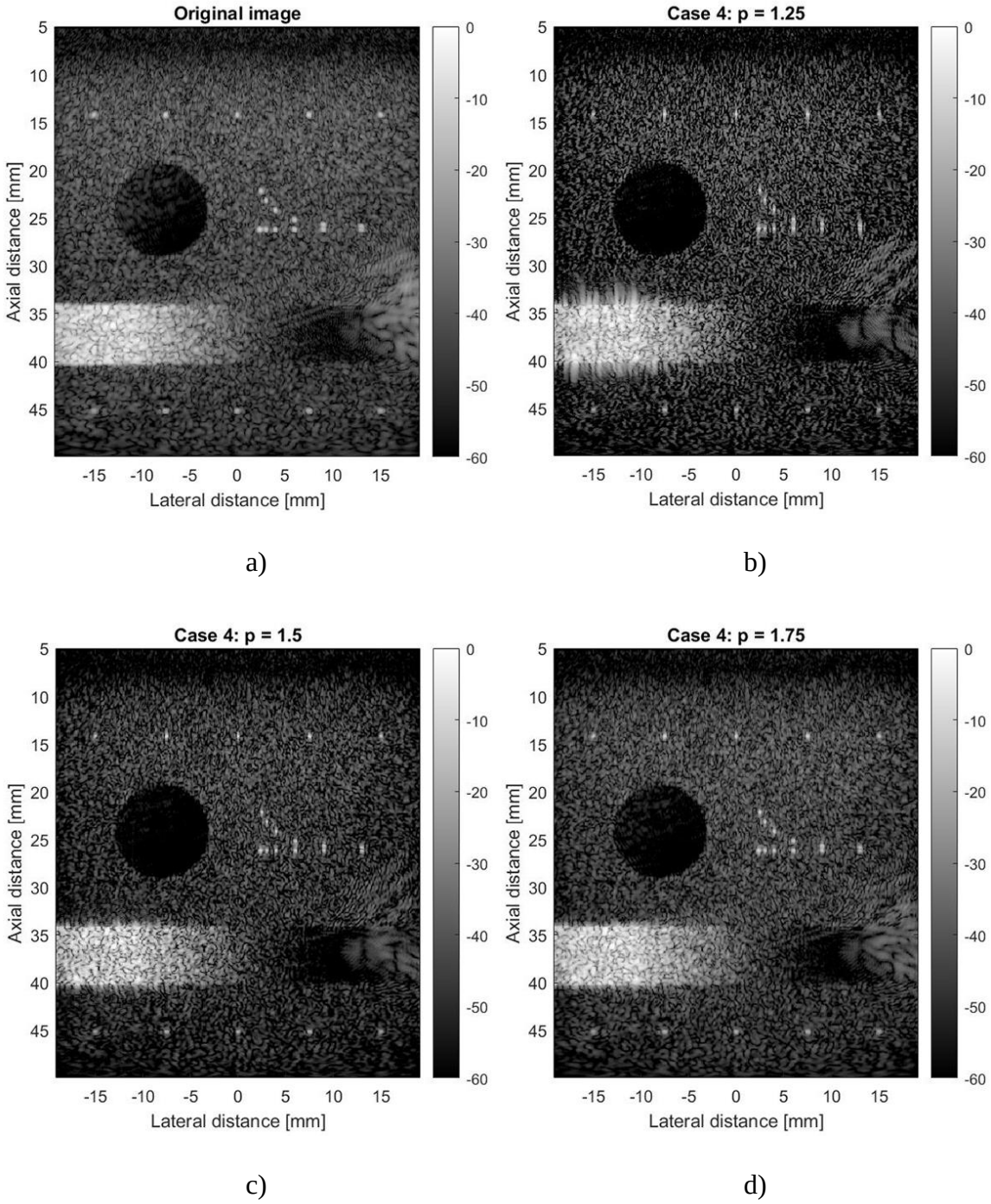

Figure 4.9. B-mode images of the simulated phantom before (a) and after deconvolution using an estimated non-stationary PSF with $p = 1.25$ (b), $p = 1.5$ (c), $p = 1.75$ (d).

Table 4.8. Image quality indicators for simulated phantom, Case 4.

	CNR, dB	Lateral resolution, mm		Axial resolution, mm		Time, s
		14 mm	45 mm	14 mm	45 mm	
a) Original image	6.6	0.36	0.53	0.38	0.41	–
b) Case 4, $p = 1.25$	5.9	0.24	0.36	0.30	**0.28**	3209.21
c) Case 4, $p = 1.5$	7	**0.21**	**0.35**	**0.24**	**0.28**	**1371.29**
d) Case 4, $p = 1.75$	**7.1**	0.28	0.44	0.30	0.36	1747.43

Carotid Artery. The results for the deconvolution of the carotid artery are presented in Figure 4.10 with the evaluation metrics shown in Table 4.9. The SSIM values indicate that all three subcases with different values of p caused a similar amount of changes. However, the subcase with $p = 1.25$ illustrates that these changes were not necessarily positive, as the algorithm introduced significant artifacts. Furthermore, computational cost is extremely high compared to the other two subcases.

In terms of TCR, both subcases with $p = 1.5$ and $p = 1.75$ produced improvements in both regions. The subcase with $p = 1.75$ achieved especially noticeable improvements by approximately 5 dB compared to the original image in both regions. Furthermore, the subcase with $p = 1.75$ surpassed the subcase with $p = 1.5$ in terms of SNR and computational speed (more than eight times faster). Overall, the subcase with $p = 1.75$ proves to be the most appealing.

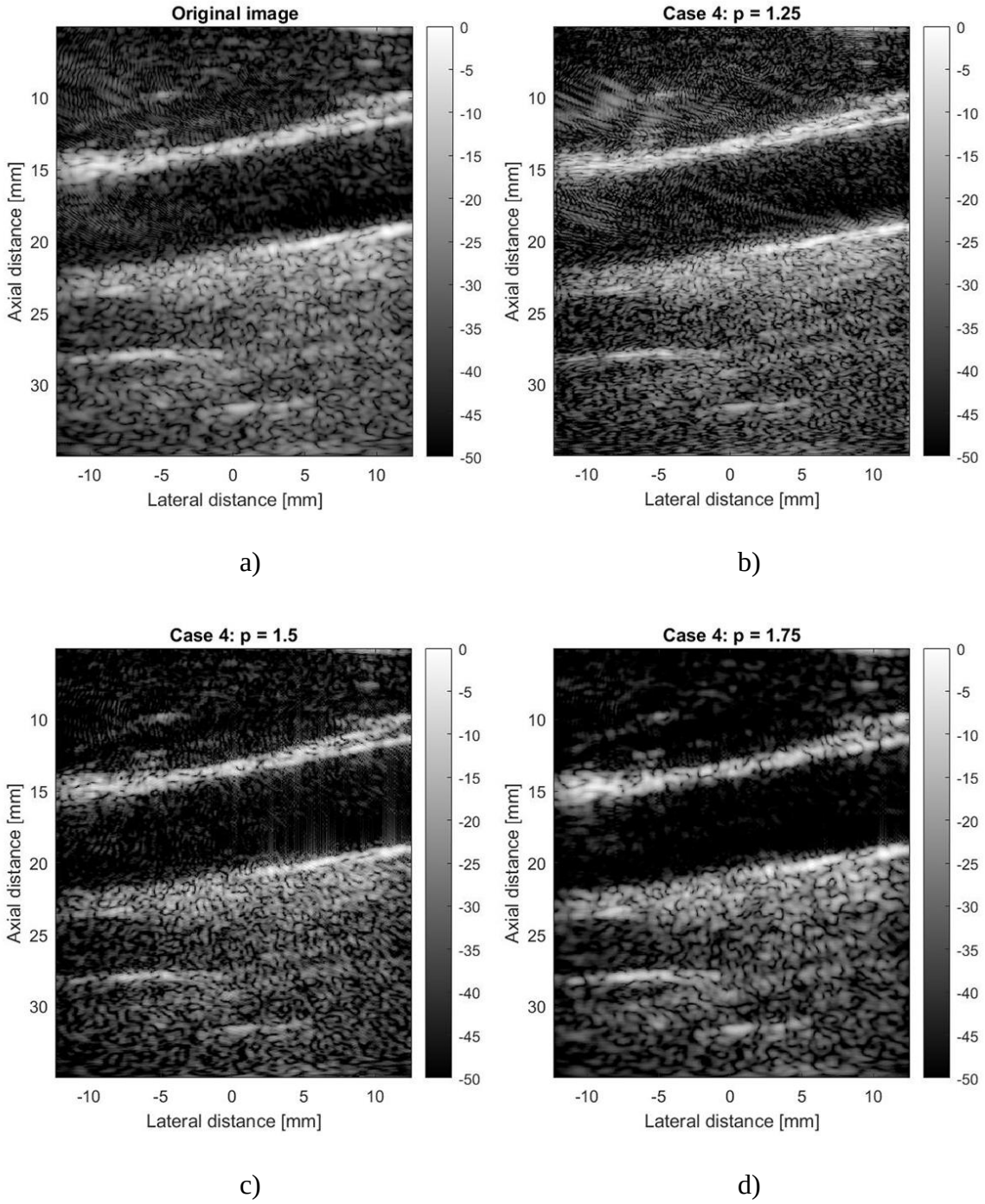

Figure 4.10. B-mode images of the carotid artery before (a) and after deconvolution using an estimated non-stationary PSF with $p = 1.25$ (b), $p = 1.5$ (c), $p = 1.75$ (d).

Table 4.9. Image quality indicators for carotid artery, Case 4.

	SSIM	PSNR, dB	SNR – 1st region	SNR – 2nd region	TCR – 1st region, dB	TCR – 2nd region, dB	Time, s
a) Original image	Ref.	Ref.	**42.523**	**40.651**	20.781	17.554	–
b) Case 4, $p = 1.25$	0.8392	30.006	30.629	27.21	21.872	14.552	3027.45
c) Case 4, $p = 1.5$	0.8521	31.404	28.323	28.288	22.009	22.205	2019.57
d) Case 4, $p = 1.75$	0.8734	34.795	32.072	31.508	**25.797**	**22.502**	**237.06**

4.6. Comparative Summary

Based on the previously described observations, performing the ℓ_p-norm minimization using $p = 1.25$ was very expensive computationally but did not produce superior results. Therefore, the subcases that used the value of $p = 1.25$ are excluded from our discussion in the sequel.

PICMUS Phantom. Table 4.10 provides the evaluation summary of the noteworthy subcases for the PICMUS simulated phantom. As we can see, in terms of axial resolution, the BD-RPCA algorithm is able to outperform all of the other algorithms under consideration. Furthermore, it provides the best result for lateral resolution at 14-mm depth. On the other hand, the BD-RPCA algorithm gives the worst CNR = 1.3 dB, which is much lower than 6.6 dB measured on the original image. Using the estimated non-stationary PSF with $p = 1.5$ achieves the superior lateral resolution at 45-mm depth and the second-best CNR value of 7 dB (the highest CNR = 7.1 dB is only 1% better). However, its computational cost is 191 times higher than that of the BD-RPCA alternative.

Table 4.10. Summary of image quality indicators for simulated phantom.

	CNR, dB	Lateral resolution, mm		Axial resolution, mm		Time, s
		14 mm	45 mm	14 mm	45 mm	
Original image	6.6	0.36	0.53	0.38	0.41	–
Case 1, $p = 1.5$	7	0.30	0.41	0.27	0.26	21.92
Case 1, $p = 1.75$	5.5	0.34	0.47	0.31	0.31	41.51
Case 2, $p = 1.5$	7	0.25	0.47	0.23	0.30	21.19
Case 2, $p = 1.75$	5.7	0.29	0.49	0.29	0.33	35.84
Case 3, $\lambda = 0.375, \rho = 0.5, \mu = 10^{-6}$	1.3	**0.20**	0.48	**0.16**	**0.21**	**7.17**
Case 4, $p = 1.5$	7	0.21	**0.35**	0.24	0.28	1371.29
Case 4, $p = 1.75$	**7.1**	0.28	0.44	0.30	0.36	1747.43

Carotid Artery. Table 4.11 provides the evaluation summary for the carotid artery, and Figure 4.11 plots the TCR values under consideration. In the previous sections, the reported SSIM and PSNR values were used to compare the normalized envelope of the deconvolved RF data to the normalized envelope of the RF data before deconvolution. In this section, however, our reference image is different: we compare all the images to the one obtained using the BD-RPCA algorithm with $\lambda = 0.0003, \rho = 1, \mu = 10^{-8}$, which gives the best TCR values of 26.621 and 25.576 dB for the first and second regions, respectively.

Table 4.11 shows that the second-best TCR values of 25.797 and 22.502 dB (for the first and second regions, respectively) are due to the deconvolution approach using the estimated non-stationary PSF with $p = 1.75$. The corresponding SSIM value for this subcase is 0.9146, which is the highest among the algorithms under consideration. The only other approach that gets close to this value is the BD-RPCA algorithm with $\lambda = 0.00003, \rho = 1, \mu = 10^{-8}$, which gives the SSIM value of 0.9138. However, its TCR values are noticeably lower.

The next metric that one might be interested in is SNR. In our particular case, the

SNR values not only exhibit significant swings (unlike more stable TCR values), but also are hard to interpret. For example, the original image in Figure 4.7 (b) offers high SNR values of 42.523 and 40.651 for the two regions of interest. They are better by at least 8 than those measured in Figure 4.7 (b), but the latter is arguably a better-quality image. For this reason, one can use PSNR values for the entire image instead, as opposed to the SNR values for two specific image regions. In terms of PSNR, the BD-RPCA algorithm with $\lambda = 0.00003, \rho = 1, \mu = 10^{-8}$ achieves the best results with the PSNR value of 37.723 dB. The deconvolution approach using the estimated non-stationary PSF with $p = 1.75$ shows the second-best PSNR values of 34.823 dB.

Lastly, it is important to compare all the cases under consideration in terms of their computational speed. Among the approaches that perform blind deconvolution, the clear winner is the BD-RPCA method that runs under 4 seconds, according to Table 4.11. The next fastest algorithm takes over 12 seconds (stationary PSF subcase with $p = 1.5$), while the slowest algorithm takes over 2000 seconds (non-stationary PSF subcase with $p = 1.5$). It should be noted, that the reported running times include only the deconvolution process, as mentioned in Section 4.1. If we were to include the time taken to estimate the PSF (which exceeded 100 seconds in our blind deconvolution experiments), the non-blind deconvolution approach would have the lowest computational cost (not requiring any calculations associated with PSF estimation based on the input data). This can be viewed as a benefit of non-blind deconvolution, assuming that the PSF is data-independent and given in advance.

Table 4.11. Summary of image quality indicators for carotid artery.

	SSIM	PSNR, dB	SNR – 1st region	SNR – 2nd region	TCR – 1st region, dB	TCR – 2nd region, dB	Time, s
Original image	0.7695	32.652	42.523	40.651	20.781	17.554	–
Case 1, $p = 1.5$	0.858	30.252	39.599	40.085	19.652	20.839	12.34
Case 1, $p = 1.75$	0.8893	34.714	42.188	41.333	21.34	19.47	18.02
Case 2, $p = 1.5$	0.7738	28.207	**42.808**	**41.952**	22.016	20.201	12.53
Case 2, $p = 1.75$	0.8156	30.722	35.613	34.969	22.408	20.529	23.41
Case 3, $\lambda = 0.00003, \rho = 1, \mu = 10^{-8}$	0.9138	**37.723**	38.894	38.068	22.962	20.522	**3.38**
Case 3, $\lambda = 0.0003, \rho = 1, \mu = 10^{-8}$	Ref.	Ref.	32.489	32.17	**26.621**	**25.576**	3.42
Case 4, $p = 1.5$	0.8591	31.648	28.323	28.288	22.009	22.205	2019.57
Case 4, $p = 1.75$	**0.9146**	34.823	32.072	31.508	25.797	22.502	237.06

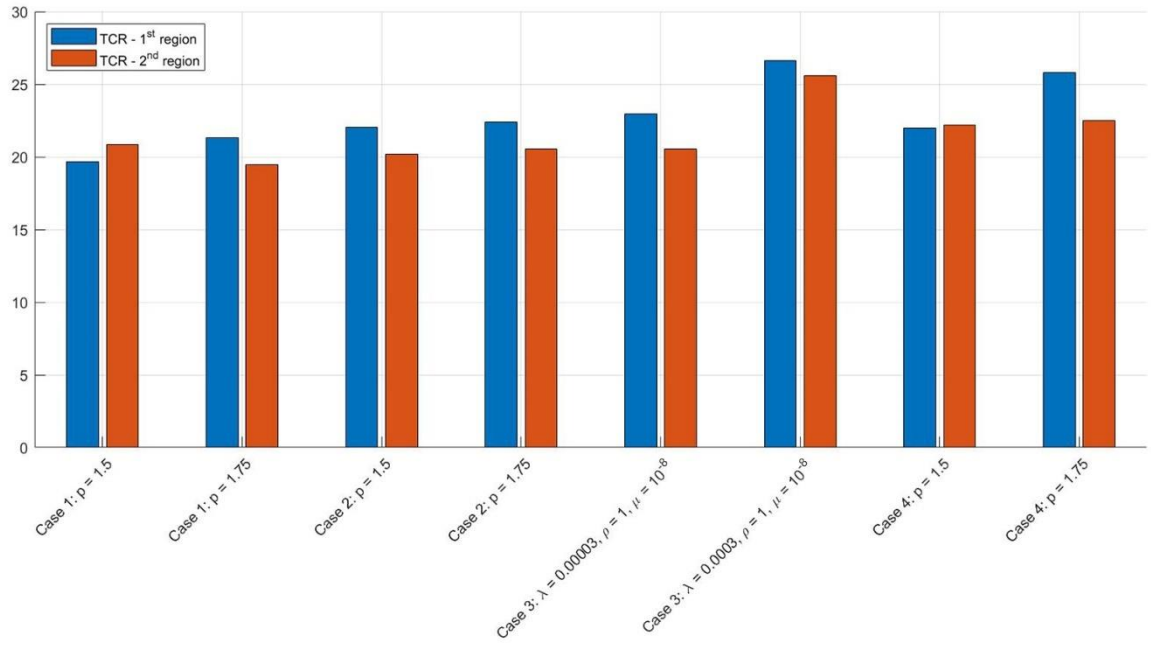

Figure 4.11. TCR values for region 1 and region 2.

To conclude this summary, we can say that different datasets might require different algorithms to achieve the best performance. For example, the algorithm

proposed in [41] outperformed other algorithms when deconvolving the PICMUS simulated phantom data. At the same time, its excessive computational complexity due to the use of the non-stationary blur modeling raises the question of whether it is worth taking such an expensive computational route to achieve desired image quality improvements. On the other hand, the BD-RPCA algorithm surpassed other algorithms when deconvolving the carotid artery data by striking a good balance between promoting sparsity and low-rankness. In other words, none of the evaluated algorithms can be considered as the best approach to all deconvolution problems.

Chapter 5: Conclusion and Future Work

5.1. Concluding Remarks

This project focuses on the problem of blind deconvolution in ultrasound imaging and features state-of-the-art methods that describe different approaches to solve this problem. We studied two papers [41] and [42] as our starting point, based on which we were able to adapt the BD-RPCA algorithm to our goal of enhancing individual 2D beamformed RF data frames via deconvolution. This work presents the evaluation results of four different approaches, including the adapted BD-RPCA, in terms of their impact on the image quality and their running time cost. The deconvolved images of the PICMUS simulated phantom and *in vivo* carotid artery were assessed based on the CNR, FWHM, SSIM, PSNR, SNR, and TCR values. We have also evaluated the impact of different settings for algorithmic hyperparameters, such as p, λ, ρ, and μ.

The deconvolution approach with the non-stationary PSF operator, proposed in [41], achieved very good image quality improvements for both image types. Unfortunately, despite its impressive imaging performance, its computational time turned out to be the worst by a wide margin among the other alternatives. On the other hand, our adapted BD-RPCA algorithm has demonstrated the best computational time by a wide margin. Despite its low computational complexity, it was able to produce competitive results for both PICMUS simulated phantom and carotid artery datasets. Its weakness was the worst CNR value obtained for the PICMUS phantom image. Its strength was the best TCR values obtained for the carotid artery image.

5.2. Future Directions

During this research, we emphasized deconvolution that targeted the sparse

component of the image. However, it would be worthwhile to explore other approaches such as deconvolution targeting the low-rank component of the image or performing deconvolution on both components separately before combining them.

One of the future research directions could be based on the work [61] written by E. Soubies *et al*. In this paper the authors propose a MATLAB library that deals with solving inverse problems, which could be adapted to the deconvolution problem at hand.

Another interesting direction for future research could pursue implementing an artificial neural network (ANN) to perform image reconstruction and enhancement based solely on a single image or features learned from other images during training [62], [63], [64], [65]. With the growth in popularity and abilities of ANNs in recent years, it is only a matter of time until the ANN-based approaches become the mainstream method for improving the quality of ultrasound images.

Bibliography

[1] M. A. Averkiou, "Tissue Harmonic Imaging," Proc. IEEE International Ultrasonics Symposium (IUS), vol. 2, pp. 1563-1572, Oct 2000.

[2] R. W. Cootney, "Ultrasound Imaging: Principles and Applications in Rodent Research," ILAR Journal, vol. 42 (3), pp. 233-247, Jan 2001.

[3] G. F. Margrave, and M. Lamoureux, Numerical Methods of Exploration Seismology with Algorithms in MATLAB, Cambridge: Cambridge University Press, Jan 2019.

[4] P. Suetens, Fundamentals of Medical Imaging, (3rd ed.), Cambridge: Cambridge University Press, Jul 2017.

[5] H. Marzougui, "Efficient Sensor Array Subsampling for Plane-Wave Ultrasound Imaging," Department of Electrical and Computer Engineering, University of Victoria, Master's thesis, May 2020.

[6] F. Dunn, "Attenuation and Speed of Ultrasound in Lung," Journal of the Acoustical Society of America, vol. 56 (5), pp. 1638-1639, Nov 1974.

[7] B. Stern, The Basic Concepts of Diagnostic Ultrasound, Yale-New Haven Teachers Institute, 1, Apr 2005.

[8] P. Younger, The Gale Encyclopedia of Medicine, (4th edition), Farmington Hills, Aug 2015.

[9] R. S. Cobbold, Foundations of Biomedical Ultrasound, Oxford: Oxford University Press, Sep 2006.

[10] D. T. Tzou, *et al*, "Ultrasound Use in Urinary Stones: Adapting Old Technology for A Modern-day Disease," Journal of Endourology, vol. 31 (S1), Apr 2017.

[11] A. Carovac, F. Smajlovic, and D. Junuzovic. “Application of Ultrasound in Medicine,” Acta Informatica Medica, vol. 19 (3), pp. 168-171, Sep 2011.

[12] H. K. Wang, *et al*, “B-flow Ultrasonography of Peripheral Vascular Diseases,” Journal of Medical Ultrasound, vol. 13 (4), pp. 186-195, Jan 2005.

[13] R. H. Wachsberg, “B-flow Imaging of the Hepatic Vasculature: Correlation with Color Doppler Sonography,” American Journal of Roentgenology, vol. 188 (6), Jun 2007.

[14] G. Stetten, *et al*, “C-Mode Real-time Tomographic Reflection for a Matrix Array Ultrasound Sonic Flashlight,” Academic Radiology, vol. 12 (5), pp. 535-543, May 2005.

[15] T. Lloyd, *et al*, “Diaphragmatic Paralysis: the Use of M-mode Ultrasound for Diagnosis in Adults,” Spinal Cord, vol. 44 (8), pp. 505-508, Aug 2006.

[16] T. J. DuBose, and A. L. Baker, “Confusion and Direction in Diagnostic Doppler Sonography,” Journal of Diagnostic Medical Sonography, vol. 25 (3), pp. 173-177, May 2009.

[17] H. C. Shin, *et al*, “Sensitivity to Point Spread Function Parameters in Medical Ultrasound Image Deconvolution,” Ultrasonics, vol. 49 (3), pp. 344-357, Mar 2009.

[18] Z. H. Cho, J. P. Jones, and M. Singh, Foundations of Medical Imaging. New York, Wiley, Sep 1993.

[19] T. L. Szabo, Diagnostic Ultrasound Imaging: Inside Out. Academic Press, Sep 2004.

[20] H. Feigenbaum, W. F. Armstrong, and T. Ryan, Feigenbaum's Echocardiography: Physics and Instrumentation, Lippincott Williams & Wilkins, pp. 29-32, Feb 2012.

[21] H. A. Akbar, and D. Rakhmatov. “Efficient Angle Selection for Coherent Plane Wave Compounding,” Proc. IEEE International Ultrasonics Symposium (IUS), pp. 2355-2357, Oct 2019.

[22] M. Ali, D. Magee, and U. Dasgupta, “Signal Processing Overview of Ultrasound Systems for Medical Imaging,” SPRAB12, Texas Instruments, Nov 2008.

[23] S. Stergiopoulos (ed.), Advanced Signal Processing Handbook: Theory and Implementation for Radar, Sonar, and Medical Imaging Real Time Systems, CRC Press, Sep 2017.

[24] J. M. Blackledge, Digital Image Processing: Mathematical and Computational Methods, Horwood Publishing, Nov 2005.

[25] J. H. Grace, and A. Young, The Algebra of Invariants, Chelsea Publishing, 1903.

[26] O. Michailovich and A. Tannenbaum, “Blind Deconvolution of Medical Ultrasound Images: A Parametric Inverse Filtering Approach,” Proc. IEEE Transactions on Image Processing, vol. 16 (12), pp. 3005-3019, Dec 2007.

[27] J. Dey, and M. K. Hasan, “Ultrasonic Tissue Reflectivity Function Estimation Using Correlation Constrained Multichannel Films Algorithm with Missing RF Data,” Biomedical Physics & Engineering Express, vol. 4 (4), Jun 2018.

[28] S. W. Smith, The Scientist and Engineer's Guide to Digital Signal Processing, California Technical Publishing, 2006.

[29] W. S. Lu, “ECE-534 Course Notes: Application of Digital Signal Processing Techniques,” Department of Electrical and Computer Engineering, University of Victoria, 2018.

[30] Y. Liu, *et al*, “Super-resolution Ultrasound Imaging by Sparse Bayesian Learning Method,” IEEE Access, vol. 7, pp. 47197-47205, Apr 2019.

[31] Y. Liu, *et al*, "Effect of PSF on Super-resolution Ultrasound Imaging Implemented by bSOFI Method," Optics in Health Care and Biomedical Optics VIII, vol. 10820, Oct 2018.

[32] M. Sakhaei, A. Mahloojifar, and A. Malek. "Optimization of Point Spread Function in Ultrasound Arrays," Ultrasonics, vol. 44 (2), pp. 159-165, Feb 2006.

[33] N. Wiener, "Extrapolation, Interpolation, and Smoothing of Stationary Time Series with Engineering Applications," MIT Press, vol. 8, 1949.

[34] T. O'Haver, "Intro to Signal Processing-deconvolution," University of Maryland at College Park, Retrieved, Jul 2008.

[35] J. Ng, *et al*, "Modeling Ultrasound Imaging as a Linear, Shift-variant System," IEEE Transactions on Ultrasonics, Ferroelectrics, and Frequency Control, vol. 53 (3), pp. 549-563, Mar 2006.

[36] J. Ng, *et al*, "Wavelet Restoration of Medical Pulse-echo Ultrasound Images in an EM Framework," IEEE Transactions on Ultrasonics, Ferroelectrics, and Frequency Control, vol. 54 (3), pp. 550-568, Mar 2007.

[37] J. Ng, *et al*, "Wavelet Restoration of Three-dimensional Medical Pulse-echo Ultrasound Datasets in an EM Framework," Acoustical Imaging, Springer, Dordrecht, pp. 403-408, Jan 2009.

[38] D. Kundur, and D. Hatzinakos. "Blind Image Deconvolution," IEEE Signal Processing Magazine, vol. 13 (3), pp. 43-64, May 1996.

[39] S. Chaudhuri, R. Velmurugan, and R. Rameshan, Blind Image Deconvolution: Methods and Convergence, Springer International Publishing, Aug 2014.

[40] P. Campisi, and K. Egiazarian, Blind Image Deconvolution: Theory and Applications, CRC Press, Dec 2017.

[41] A. Besson, *et al*, "A Physical Model of Non-stationary Blur in Ultrasound Imaging," IEEE Transactions on Computational Imaging, vol. 5 (3), pp. 381-394, Sep 2019.

[42] D. Pham, *et al*, "Joint Blind Deconvolution and Robust Principal Component Analysis for Blood Flow Estimation in Medical Ultrasound Imaging," IEEE Transactions on Ultrasonics, Ferroelectrics, and Frequency Control, vol. 68 (4), pp. 969-978, Apr 2021.

[43] O. Michailovich, A. Basarab, and D. Kouame, "Iterative Reconstruction of Medical Ultrasound Images Using Spectrally Constrained Phase Updates," Proc. IEEE International Symposium on Biomedical Imaging (ISBI), pp. 1765-1768, Apr 2019.

[44] T. Taxt, "Restoration of Medical Ultrasound Images Using Two-Dimensional Homomorphic Deconvolution," IEEE Transactions on Ultrasonics, Ferroelectrics, and Frequency Control, vol. 42 (4), pp. 543-554, Jul 1995.

[45] O. Michailovich and D. Adam, "A Novel Approach to the 2-D Blind Deconvolution Problem in Medical Ultrasound," IEEE Transactions on Medical Imaging, vol. 24 (1), pp. 86-104, Jan 2005.

[46] S. Boyd, *et al*, Distributed Optimization and Statistical Learning via the Alternating Direction Method Of Multipliers, Foundations and Trends in Machine Learning, vol. 3 (1), pp. 1-122, Jan 2011.

[47] H. Shen, *et al*, "High-resolution and High-sensitivity Blood Flow Estimation Using Optimization Approaches with Application to Vascularization Imaging," Proc. IEEE International Ultrasonics Symposium (IUS), pp. 467-470, Oct 2019.

[48] J. Wright, *et al*, "Robust Principal Component Analysis: Exact Recovery of Corrupted Low-rank Matrices via Convex Optimization," International Conference in Neural Information Processing Systems, vol. 58, pp. 2080-2088, Dec 2009.

[49] J. A. Jensen and N. B. Svendsen, "Calculation of Pressure Fields from Arbitrarily Shaped, Apodized, and Excited Ultrasound Transducers," IEEE Transactions on Ultrasonics, Ferroelectrics, and Frequency Control, vol. 39 (2), pp. 262-267, Mar 1992.

[50] A. Besson, *et al*. "Ultrafast Ultrasound Imaging as an Inverse Problem: Matrix-free Sparse Image Reconstruction," IEEE Transactions on Ultrasonics, Ferroelectrics, and Frequency Control, vol. 65 (3), pp. 339-355, Nov 2017.

[51] Z. Chen, A. Basarab and D. Kouame, "Compressive Deconvolution in Medical Ultrasound Imaging," IEEE Transactions on Medical Imaging, vol. 35 (3), pp. 728-737, Mar 2016.

[52] N. Zhao, *et al*, "Blind Deconvolution of Medical Ultrasound Images Using a Parametric Model for the Point Spread Function." Proc. IEEE International Ultrasonics Symposium (IUS), pp. 1-4, Sep 2016.

[53] M. Alessandrini, *et al*, "A Restoration Framework for Ultrasonic Tissue Characterization," IEEE Transactions on Ultrasonics, Ferroelectrics, and Frequency Control, vol. 58 (11), pp. 2344-2360, Nov 2011.

[54] R. Morin, *et al*, "Semi-blind Deconvolution for Resolution Enhancement in Ultrasound Imaging," Proc. IEEE International Conference on Image Processing, pp. 1413-1417, Sep 2013.

[55] L. Roquette, *et al*, "On an Analytical, Spatially-varying, Point Spread Function," Proc. IEEE International Ultrasonics Symposium (IUS), pp. 1-4, Sep 2017.

[56] A. Beck and M. Teboulle, “A Fast Iterative Shrinkage-Thresholding Algorithm for Linear Inverse Problems,” SIAM Journal on Imaging Sciences, vol. 2 (1), pp. 183-202, Sep 2009.

[57] Creatis, University of Lyon 2018, *PICMUS Evaluation Framework*, Accessed 17 July 2021, <https://www.creatis.insa-lyon.fr/EvaluationPlatform/picmus/index.html>

[58] J. A. Jensen 2021, Accessed 21 July 2021, <http://field-ii.dk/>

[59] Verasonics, Inc. 2021, Accessed 14 July 2021, <https://verasonics.com/>

[60] M. C. Van Wijk, and J. M. Thijssen. “Performance Testing of Medical Ultrasound Equipment: Fundamental vs. Harmonic Mode,” Ultrasonics, vol. 40 (1-8), pp. 585-591, May 2002.

[61] E. Soubies, *et al*. “Pocket Guide to Solve Inverse Problems with GlobalBioIm,” Inverse Problems, vol. 35 (10), Sep 2019.

[62] D. Ulyanov, A. Vedaldi, and V. Lempitsky. “Deep Image Prior,” Proc. IEEE Conference on Computer Vision and Pattern Recognition, pp. 9446-9454, Jun 2018.

[63] X. Liu, *et al*. “Deep Learning for Ultrasound Localization Microscopy,” IEEE Transactions on Medical Imaging, vol. 39 (10), pp. 3064-3078. Apr 2020.

[64] C. A. Metzler, *et al*. “Unsupervised Learning with Stein's Unbiased Risk Estimator,” arXiv Preprint, May 2018.

[65] H. K. Aggarwal, M. P. Mani, and M. Jacob. “MoDL: Model-based Deep Learning Architecture for Inverse Problems,” IEEE Transactions on Medical Imaging, vol. 38 (2), pp. 394-405, Feb 2019.

[66] G. J. O. Jameson. Summing and Nuclear Norms in Banach Space Theory. Cambridge University Press, 1987.

[67] H. Dong, J. Yu, and C. Xiao. “Dual Reweighted Lp-norm Minimization with Application in Image Denoising,” arXiv preprint, Nov 2018.